Understanding the seasonal dynamics of phytoplankton biomass and the deep chlorophyll maximum in oligotrophic environments: A Bio-Argo float investigation

Alexandre Mignot, Hervé Claustre, Julia Uitz, Antoine Poteau, Fabrizio d'Ortenzio, Xiaogang Xing

AGU PUBLICATIONS

Global Biogeochemical Cycles

RESEARCH ARTICLE
10.1002/2013GB004781

Key Points:
- A bio-optical data set is created from Bio-Argo floats in oligotrophic regions
- This data set reveals the seasonal dynamics of phytoplankton biomass
- A common mechanism is responsible for the observed seasonal dynamics

Supporting Information:
- Supplementary Text
- Figure S1

Correspondence to:
A. Mignot,
mignot@mit.edu

Citation:
Mignot, A., H. Claustre, J. Uitz, A. Poteau, F. D'Ortenzio, and X. Xing (2014), Understanding the seasonal dynamics of phytoplankton biomass and the deep chlorophyll maximum in oligotrophic environments: A Bio-Argo float investigation, *Global Biogeochem. Cycles*, *28*, 856–876, doi:10.1002/2013GB004781.

Received 26 NOV 2013
Accepted 28 JUL 2014
Accepted article online 1 AUG 2014
Published online 22 AUG 2014

Understanding the seasonal dynamics of phytoplankton biomass and the deep chlorophyll maximum in oligotrophic environments: A Bio-Argo float investigation

Alexandre Mignot[1,2,3], Hervé Claustre[1,2], Julia Uitz[1,2], Antoine Poteau[1,2], Fabrizio D'Ortenzio[1,2], and Xiaogang Xing[4]

[1]Sorbonne Universités, UPMC Université Paris 6, UMR 7093, LOV, Observatoire Océanologique de Villefranche, Villefranche-sur-Mer, France, [2]CNRS, UMR 7093, LOV, Observatoire Océanologique de Villefranche, Villefranche-sur-Mer, France, [3]Now at Massachusetts Institute of Technology, Cambridge, Massachusetts, USA, [4]Physical Oceanography Laboratory, Ocean University of China, Qingdao, China

Abstract We deployed four Bio-Argo profiling floats in various oligotrophic locations of the Pacific subtropical gyres and Mediterranean Sea to address the seasonal phytoplankton dynamics in the euphotic layer and explore its dependence on light regime dynamics. Results show that there is a similar phytoplankton biomass seasonal pattern in the four observed oceanic regions. In the lower part of the euphotic layer, the seasonal displacement of the deep chlorophyll maximum (DCM) is light driven. During winter, the chlorophyll *a* concentration ([Chl *a*]) always increases in the upper euphotic mixed layer. This increase always results from a photoacclimation to the reduced irradiance. Depending on the location, however, the concentration can also be associated with an actual increase in biomass. The winter increase in [Chl *a*] results in an increase in irradiance attenuation that impacts the position of the isolume (level where the daily integrated photon flux is constant) and DCM, which becomes shallower. In summer when the [Chl *a*] in the upper layer decreases along with light attenuation, the DCM deepens and becomes closer to (and sometimes reaches) the nitracline, which enhances the phytoplankton biomass at the DCM. The bio-optical mechanisms and their relationship to light regimes that are revealed by the time series appear to be generic and potentially characteristic of all of the areas where a DCM forms, which is 50% of the open ocean.

1. Introduction

Oligotrophic regions are defined as areas of the global ocean where the surface chlorophyll *a* concentration ([Chl *a*]) is lower than 0.1 mg m^{-3} [*Antoine et al.*, 1996]. Usually, the vertical distribution of [Chl *a*] is not homogeneous in these areas and displays a pronounced maximum close to the base of the euphotic zone, which is called the deep chlorophyll maximum (DCM) with depths that range between 50 and 200 m [*Mignot et al.*, 2011]. The oligotrophic regions represent the largest oceanic ecosystem in the ocean and occupy 50% of the ocean surface (DCM depth $>$ 50 m in Figure 1). They are mainly formed by the five subtropical gyres of the Atlantic, Pacific, and Indian Basins as well as certain zones of the Mediterranean Sea. The nutrient supply to the euphotic zone in these oligotrophic regions is minimal, so the phytoplankton biomass and primary production are low throughout the year. Nevertheless, the size of these regions makes their contribution to the global ocean primary production potentially significant.

Because of an increase in their vertical stratification, oligotrophic regions are also considered to be expanding and intensifying while their productivity, as well as their Chl *a* content, is expected to decline [*Sarmiento et al.*, 2004; *Behrenfeld et al.*, 2006; *Polovina et al.*, 2008]. Despite their potential influence on the global ocean carbon cycle, there are large unknowns and uncertainties regarding the dynamics of phytoplankton biomass and associated carbon fluxes as well as the factors driving these dynamics in oligotrophic regions; the uncertainties partially result from the remoteness of these regions. Hence, our present understanding essentially relies on (1) remote sensing observations that are restricted to the upper ocean layer [*McClain et al.*, 2004; *D'Ortenzio and d' Alcala*, 2009; *Morel et al.*, 2010], (2) several ship-based investigations (e.g., Blogeochemistry and Optics SOuth Pacific Experiment cruise [*Claustre et al.*, 2008]), and (3) observation time series (e.g., Hawaii Ocean Time-Series (HOT) program [*Karl and Lukas*, 1996]). Additional investigations dedicated to the understanding of the variability

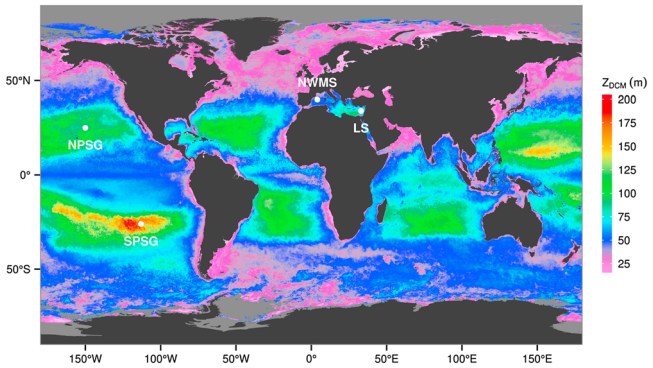

Figure 1. Annual average depth of the DCM (Z_{DCM}) for 2012. The map was produced from the annual average sea surface [Chl *a*] ($[Chl]_{surf}$) derived from MODIS using the following equation: $\log_{10}(Z_{DCM}) = 1.429 - 0.314 \cdot \log_{10}([Chl]_{surf}) + 0.099 \cdot \log_{10}([Chl]_{surf})^2$ ($r^2 = 0.84$, $n = 319$) This relationship has been established using a data set that includes Chl *a* fluorescence and accurate estimation of [Chl *a*] by high-performance liquid chromatography [*Mignot et al.*, 2011].

in phytoplankton dynamics over seasonal, interannual, and even longer time scales are required as a preliminary step toward the future assessment of the possible influences of changing environments on the productivity of oligotrophic oceanic regions.

Within oligotrophic oceans, the stratification of the water column generally prevents nutrient injections from deeper waters into the euphotic zone [*Karl*, 1999; *McClain et al.*, 2004], even during winter when the deepening of the mixed layer appears insufficient to reach and erode the nitracline (except for the western basin of the Mediterranean Sea [*Marty et al.*, 2002] and western region of the North Atlantic subtropical gyre [*Michaels and Knap*, 1996]). As a result, this quasi-permanent stratification delineates two production regimes along the vertical dimension. In the upper part of the euphotic zone, phytoplankton production is quasi-permanently nutrient limited. Additionally, the deepening of the mixed layer during winter, even if insufficient for bringing up nutrients, could potentially be responsible for a significant light limitation in phytoplankton communities [*Winn et al.*, 1995]. In the lower part of the euphotic zone and below, phytoplankton are always light limited and benefits from new nutrient injections, either through diffusion [*Lewis et al.*, 1986] or mesoscale processes such as cyclonic eddies [*Seki et al.*, 2001]. This division between the upper and lower parts is consistent with the two-layered euphotic zone conceptual model of the North Pacific oligotrophic gyre that resulted from the Vertical Transport and Exchange project time series study [*Coale and Bruland*, 1987]. It is also consistent with historical observations in the North Pacific that established the presence of distinct phytoplankton assemblages in the upper and lower euphotic zones [*Venrick*, 1988].

Satellite ocean color as well as in situ studies revealed a common seasonal pattern in the upper euphotic zone of the oligotrophic ocean. The [Chl *a*] increases every winter and decreases in summer. The cause of the winter increase is still a matter of debate. The [Chl *a*] increase might reflect a real increase in phytoplankton (carbon) biomass resulting from new nutrient availability that results from nitracline erosion [*Letelier et al.*, 1993; *Morel et al.*, 2010]. However, the [Chl *a*] increase might also result from phytoplankton photoacclimation processes in response to severe light limitation when phytoplankton are mixed from the surface to the base of the mixed layer [*Letelier et al.*, 1993; *Winn et al.*, 1995]. These two processes are not necessarily exclusive because they could simultaneously contribute to the increase in [Chl *a*] observed in winter. The lack of consensus partly results from the lack of appropriate in situ measurements (other than [Chl *a*]) of the phytoplankton biomass [*Letelier et al.*, 1993; *Morel et al.*, 2010]. One of the main objectives of this paper is to address and solve this issue.

Far from the surface layer "seen" by a satellite, the seasonal variability of phytoplankton in the lower part of the euphotic zone is even less understood. In this layer, the phytoplankton vertical distribution is characterized by a DCM, which is a typical feature of stratified open oceans. Since the seminal paper of *Cullen* [1982], the mechanisms of its formation and maintenance have been largely debated [*Kitchen and Zaneveld*, 1990; *Estrada et al.*, 1993; *Maranon et al.*, 2000; *Fennel and Boss*, 2003]. Theoretical studies appear to converge toward a general concept. The DCM may result from phytoplankton living in a contrasted gradient of two essential resources in a stratified water column, which include photon flux supplied from the surface and nutrients usually supplied from depths. The DCM may form independently of a maximum of phytoplankton carbon biomass (deep biomass maximum, DBM) because the ratio of Chl *a* concentration to phytoplankton carbon biomass increases with the acclimation of cells to reduced light.

To our knowledge, the study of *Letelier et al.* [2004] (LTL04) is the only study that has considered the seasonal dynamics of the DCM. Based on the analysis of monthly in situ profiles of downwelling irradiance, nutrients and [Chl *a*] at the A Long-term Oligotrophic Habitat Assessment (ALOHA) station (HOT program, North Pacific

Gyre), this study showed that the DCM dynamics are essentially irradiance driven. The DCM is systematically located at the level of a given isolume (the level where the daily integrated photon flux is constant) all year long. These isolumes and the DCM are deeper during summer than winter because of the combined increase of surface irradiance and decrease of light attenuation in the upper layer. The deepening of the DCM during summer is also associated with an increase in [Chl *a*] at the DCM, which is concomitant with the removal of inorganic nitrogen in the lower part of the euphotic zone and supports the hypothesis of an increase in photoautotrophic biomass production. Whether or not the concept of LTL04 can be extended to other oligotrophic regions of the global ocean remains to be investigated.

Therefore, a crucial need exists for repetitive in situ biogeochemical and bio-optical measurements to determine the seasonality of phytoplankton dynamics in the lower layer of the euphotic zone in oligotrophic oceans and better understand its role in controlling new nutrients that are trapped in this rather unknown layer. Such an understanding constitutes a prerequisite to addressing the possible influence of climate change in these regions. Nevertheless, as a result of the remoteness of the oligotrophic regions (primarily the central part of ocean basins), repetitive in situ measurements are costly and logistically demanding through classical sampling strategies (e.g., oceanographic cruises).

In the late 1990s, the physical oceanographic community promoted and then implemented the Argo program [*Roemmich et al*., 1999]. Its aim was to develop an array (~3000) of vertical profiling floats to measure the temperature and salinity of the upper 1000 to 2000 m of the water column over the entire global ocean. Recently, miniaturized bio-optical sensors have been implemented on such profiling floats that offer new observational capabilities of key biogeochemical variables [*Johnson et al*., 2010; *Xing et al*., 2011] at temporal scales that have been poorly resolved (e.g., seasonal and interannual) and in areas too remote for intensive investigations over long-term periods by ship-based platforms. We have developed Bio-Argo profiling floats that carry traditional conductivity, temperature, depth (CTD) sensors along with an array of optical sensors, such as a Chl *a* fluorometer, colored dissolved organic matter (CDOM) fluorometer, beam transmissometer that measures the particle attenuation coefficient, backscatterometer that measures the particle backscattering coefficient, and radiometer that measures downwelling irradiance. These floats are programmed to sample the euphotic zone and below at a relatively high frequency (every 5 or 10 days) and over at least 1 year.

In 2008, four Bio-Argo profiling floats were deployed: one in the vicinity of Hawaiian Islands in the North Pacific Subtropical Gyre (NPSG), one in the vicinity of Easter Island in the South Pacific Subtropical Gyre (SPSG), one in the Levantine Sea (LS), and one in the northwestern Mediterranean Sea (NWMS) (Figure 1). The NPSG and SPSG are oligotrophic environments in a strict sense. However, the generally admitted oligotrophic status of the Mediterranean Sea [*McGill*, 1969; *Dugdale and Wilkerson*, 1988] might be challenged at the seasonal scale, especially alongshore and in some northwestern zones [*Bosc et al*., 2004; *D'Ortenzio and d' Alcala*, 2009]. Therefore, the present investigation potentially covers a wide range of permanent as well as intermittent oligotrophic environments.

The general objective of the present study is to perform a comparative investigation of the seasonal dynamics in the vertical distribution of the phytoplankton biomass in these distinct oligotrophic environments using these "long" time series of physical and bio-optical parameters. Within this general objective, three main topics are addressed: (1) we investigate to what degree the increase of recurrent surface [Chl *a*] during winter (as seen from satellite remote sensing) results from a true biomass increase versus a photoacclimation "artifact"; (2) we then evaluate if the conceptual scheme of LTL04 for the DCM seasonal dynamics (depth and magnitude) at the ALOHA station can be applied to other oligotrophic environments; and (3) we finally analyze what type of functional links exists between the upper (upper euphotic mixed) and lower (lower euphotic-DCM) layers of the euphotic zone of such systems and determine their evolution at the seasonal scale.

2. Methods

2.1. Bio-Argo Float

The PROVOR (NKE) is one of the profiling floats used as a part of the Argo program. It is traditionally equipped with a Sea-Bird Electronics SBE41CP CTD and is capable of acquiring measurements from 1000 m up to the surface every 10 days for a period of ~3 years. Once the float surfaces, data are transmitted in real time

Table 1. Symbols Used in This Study

Symbol	Definition	Units
MLD	mixed layer depth	m
Z_{pd}	first penetration depth	m
Z_{DCM}	depth of the DCM	m
[Chl *a*]	chlorophyll *a* concentration	mg m^{-3}
$[Chl]_{surf}$	median of [Chl *a*] in the first penetration depth	mg m^{-3}
$[Chl]_{DCM}$	[Chl *a*] concentration at the DCM	mg m^{-3}
c_p	beam attenuation coefficient at 660 nm	m^{-1}
c_{psurf}	median of c_p in the first penetration depth	m^{-1}
c_{pDCM}	c_p at the DCM	m^{-1}
c_p*	ratio of c_p to [Chl *a*]	m^2 mg^{-1}
c_{psurf}*	median of c_p* in first penetration depth	m^2 mg^{-1}
c_{pDCM}*	c_p* at the DCM	m^2 mg^{-1}
b_{bp}	particulate backscattering coefficient at 532 nm	m^{-1}
b_{bpsurf}	median of b_{bp} in first penetration depth	m^{-1}
b_{bpDCM}	b_{bp} at the DCM	m^{-1}
b_{bp}*	ratio of b_{bp} to [Chl *a*]	m^2 mg^{-1}
b_{bpsurf}*	median of b_{bp}* in first penetration depth	m^2 mg^{-1}
b_{bpDCM}*	b_{bp}* at the DCM	m^2 mg^{-1}
PAR	photosynthetically available radiation	mol quanta m^{-2} d^{-1}
PAR(0^-)	PAR under the sea surface	mol quanta m^{-2} d^{-1}
PAR_{ML}	average value of the integral of the PAR(z) profile over the mixed layer	mol quanta m^{-2} d^{-1}
PAR_{DCM}	PAR at the DCM	mol quanta m^{-2} d^{-1}
K_d(PAR)	diffuse attenuation coefficient of PAR	m^{-1}

through Argos telemetry. The PROVBIO float is an improved version of the PROVOR float dedicated to bio-optical and biogeochemical studies through the integration of a suite of additional optical sensors: WET Labs C-Rover transmissometer at 660 nm; Satlantic OC4 Radiometer measuring downwelling irradiance at 412, 490, and 555 nm; and WET Labs Environmental Characterization Optics triplet puck composed of a Chl *a* fluorometer (excitation at 470; emission at 695 nm), CDOM fluorometer (excitation at 370; emission at 460 nm), and backscattering sensor at 532 nm. The diversity of measurements performed by the PROVBIO float together with the 1 m vertical resolution imposes to replace Argos with Iridium telemetry (which has a higher band pass). Iridium also offers the capability of modifying the float mission parameters, such as the sampling strategy, in quasi real time.

2.2. Float Deployments and Mission

Since 2008, eight PROVBIO floats have been deployed and collected data over a time period of approximately 2 years (see Table 1 in *Xing et al*. [2011]). As part of this study, we used four of these floats deployed in four different oceanic regions (Figure 2). Two floats were deployed in the Mediterranean Sea in the northwestern basin and eastern Levantine Basin (Figures 2b and 2d show floats that denoted NWMS and LS, respectively). One float was located north of Hawaii (Figure 2a; NPSG) in the eastern sector of the North Pacific Subtropical Gyre. The fourth float sampled the waters surrounding Easter Island within the hyperoligotrophic South Pacific Subtropical Gyre (Figure 2c; SPSG).

The nominal mission of these floats included the acquisition of a CTD profile from a depth of 1000 m up to the surface, whereas the bio-optical sensors acquired data from approximately 400 m up to the surface. The optical sampling resolution was 1 m. The CTD sampling resolution was 3 m from the surface to 400 m and 25 m from 400 m to 1000 m. The upward casts of the NWMS and LS floats were programmed every 5 days, whereas the upward casts of the NSPSG and NPSG floats were programmed every 10 days. In some occasions, three casts per day were programmed (sunrise, noon, and sunset) to address short-term variability and biogeochemical fluxes. Here only noon casts are analyzed. All of the floats acquired data for more than 1 year. In this study, we present and analyze a continuous 1 year time series for each float.

2.3. Processing Raw Data

The CTD data were quality controlled by the standard Argo protocol [*Wong et al*., 2010].

After the dark counts were subtracted from the raw signal, the Chl *a* fluorescence was first converted into Chl *a* concentration through the scale factor provided by the manufacturer. This scale factor (in units of mg m^{-3} $counts^{-1}$) resulted from a calibration based on *Thalassiosira weissflogii* cultures. The resulting [Chl *a*] profiles were subsequently cleaned of spikes and out-of-range values through a real-time dedicated quality control procedure [*International Ocean Colour Coordinating Group*, 2011].

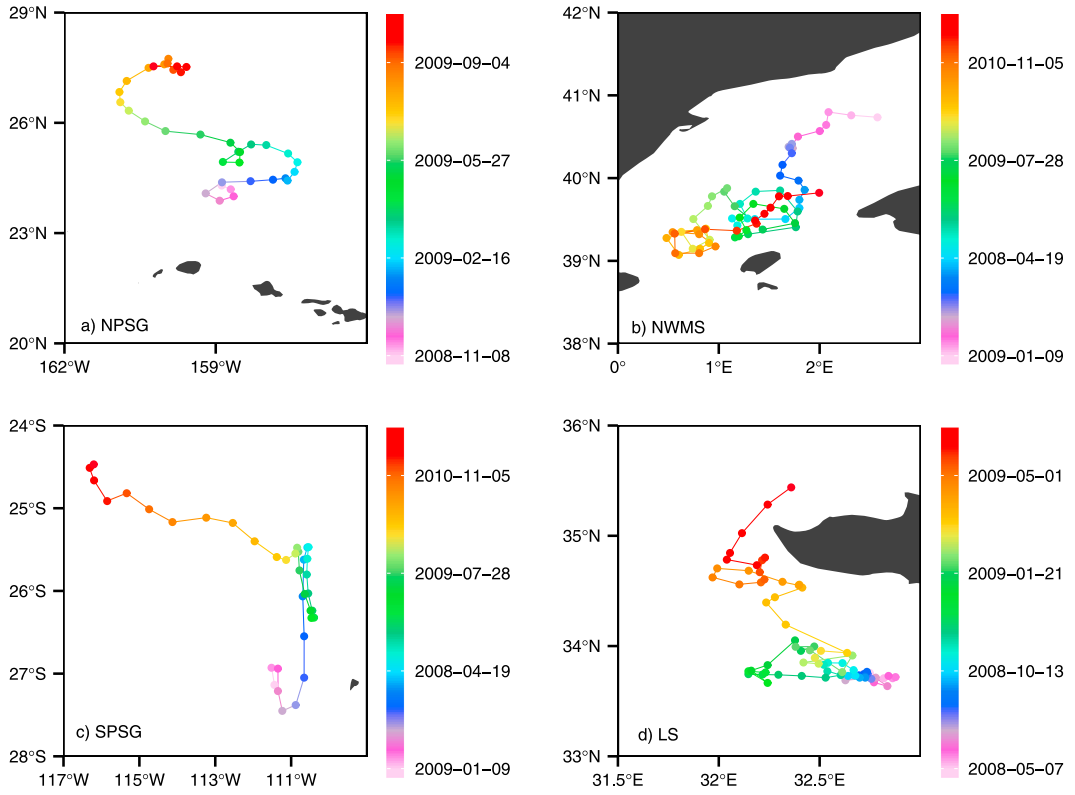

Figure 2. Trajectory of the four floats used in this study as a function of date (color coded). The dots represent the location of the sampling (optical and CTD) profiles used in this study.

The beam transmission, T (%), was transformed into the beam attenuation coefficient, c (m^{-1}), using the following relationship:

$$c = -\frac{1}{x}\ln\frac{T}{100} \tag{1}$$

where x is the transmissometer path length (25 cm). The beam attenuation coefficient c corresponds to the sum of the attenuation coefficients of seawater (0.364 m^{-1} at 660 nm), CDOM (negligible at this wavelength in oligotrophic waters [*Bricaud et al.*, 1981]), and particles. At 660 nm, the particle beam attenuation coefficient, c_p (m^{-1}), is retrieved by subtracting the water contribution to c; c_p is assumed to be a proxy of particle mass concentration.

The backscattering sensor carried by the PROVBIO float provides the volume scattering function of particles at an angle of 117° and wavelength of 532 nm (β(117°, 532)). The β(117°, 532) represents the sum of the particle scattering plus the water molecular scattering. To retrieve the volume scattering function of particles β_p(117°, 532), the volume scattering function of water β_w(117°, 532) (with β_w(117°, 532) obtained according to the relationship in *Morel* [1974]) is subtracted from β(117°, 532). The particulate backscattering coefficient, b_{bp}(532) (m^{-1}), is determined by estimating the sole measurement of β_p(117°, 532) using an X factor:

$$b_{bp}(532) = 2\pi X\beta_p(117°,\ 532) \tag{2}$$

The X factor has been determined by *Boss and Pegau* [2001] to be 1.1 at any wavelength. Hereafter, b_{bp}(532) will be denoted as b_{bp}.

Finally, the optical profiles were visually inspected on a case-by-case basis. They were deemed inappropriate and thus omitted from further analysis if the shape of the vertical profile was suspicious (i.e., deep values greater than surface values).

2.4. From Optical Measurements to Biogeochemical Data

Factory calibration of the Chl *a* fluorometer based on the use of phytoplankton culture only produces a crude estimation of the Chl *a* concentration. The Chl *a* concentration-fluorescence relationship depends on the taxonomic composition and physiological status of natural phytoplankton populations that are obviously not accounted for through culture-based calibrations. When possible, alternative methods should be used to retrieve more accurate Chl *a* concentrations. A new method was recently developed that makes use of simultaneous measurements of fluorescence and downward irradiance profiles at 490 nm [*Xing et al*., 2011]. This method allows for a more accurate retrieval of Chl *a* concentrations than the factory-based calibration and simultaneously provides a noise-free (cloudless) radiometric profile. The method of *Xing et al*. [2011] was applied to the time series of float measurements at noon to retrieve the scaling factor required for the calibration of the fluorometer. For each float, the raw fluorescence profiles were then calibrated to [Chl *a*] using the mean scaling factor of the time series.

As a result of the vertical position of the transmissometer, sinking material progressively accumulates on the detection window over time [*Bishop and Wood*, 2009]. To account for the drift of c_p that results from this accumulation, c_p was corrected assuming that c_p equals zero at ~350 m [*Loisel and Morel*, 1998; *Claustre et al*., 1999]. Therefore, the median of the last 10 deepest measurements was subtracted from each value of the profile.

Particles in the 0.5–20 μm size range make a dominant contribution to the c_p signal [*Morel*, 1973; *Stramski and Kiefer*, 1991; *Durand and Olson*, 1996]. This range encompasses phytoplankton, heterotrophs, as well as detrital and inorganic particles. The c_p value was usually related to particulate organic carbon (POC) concentration through a linear relationship [*Gardner et al*., 1993; *Loisel and Morel*, 1998; *Claustre et al*., 1999]. However, the c_p-POC relationship is not universal, and regional differences have been reported in previous studies [*Fennel and Boss*, 2003]. These differences also raised controversies regarding their real or methodological origins [*Bishop*, 1999; *Gardner et al*., 2006; *Cetinic et al*., 2012]. Here the conversion of c_p into POC could be critical when comparing absolute values between the four oceanic regions. *Behrenfeld and Boss* [2003] argued that c_p would be a better proxy for phytoplankton biomass than for POC. Other studies also support the use of c_p as a phytoplankton biomass proxy [*Behrenfeld and Boss*, 2006; *Dall'Olmo et al*., 2009, 2011; *Westberry et al*., 2010]. Following this suggestion, we hypothesized that the seasonal changes in c_p tracked the changes in phytoplankton biomass, which indicated that the relative contribution of phytoplankton to c_p was invariant over seasons. In our study, c_p was not converted to a carbon equivalent; instead, it was used as an index of phytoplankton biomass. Therefore, the Chl *a*-specific attenuation coefficient, c_p^*, calculated as the ratio of c_p to [Chl *a*], was used as a proxy of the phytoplankton biomass to Chl *a* ratio and may reveal changes in phytoplankton physiology. Depth-dependent changes in c_p^* have indeed been shown to follow changes in intracellular pigment concentration resulting from photoacclimation [*Mitchell and Kiefer*, 1988; *Kitchen and Zaneveld*, 1990; *Mitchell and Holmhansen*, 1991; *Morel et al*., 1993].

The PROVBIO float deployed in the Levantine Sea carried a defective transmissometer. To overcome this problem, we followed the approach developed by *Behrenfeld et al*. [2005] for global estimations of phytoplankton biomass from satellite retrievals of b_{bp}, and used b_{bp} (instead of c_p) as an index of phytoplankton biomass. In this case, b_{bp}^* (similar to c_p^*) was also used as a proxy of the phytoplankton biomass to Chl *a* ratio.

For the determination of the vertical profile of daily photosynthetically available radiation (PAR, mol quanta $m^{-2}\,d^{-1}$), we used the method described below. The PAR just below the sea surface, PAR(0^-), was first determined as follows:

$$\mathrm{PAR}(0^-) = E_d(490,\ 0^-, t_{\mathrm{noon}}) \times f \tag{3}$$

where $E_d(490, 0^-, t_{\mathrm{noon}})$ (μW $cm^{-2}\,nm^{-1}$) is the noise-free downward irradiance at 490 nm, measured just beneath the sea surface at noon [*Xing et al*., 2011]. The conversion factor f enables the transformation of $E_d(490, 0^-, t_{\mathrm{noon}})$ to PAR(0^-)(mol quanta $m^{-2}\,d^{-1}$). This conversion factor is calculated as follows:

$$f = \frac{\mathrm{PAR}(0^-)^{\mathrm{mod}}}{E_d(490,\ 0^-, t_{\mathrm{noon}})^{\mathrm{mod}}} \tag{4}$$

where $E_d(490, 0^-, t_{\mathrm{noon}})^{\mathrm{mod}}$ is the clear-sky modeled value of $E_d(490, 0^-, t_{\mathrm{noon}})$ for the same location and time of the day as the measurement and PAR(0^-)$^{\mathrm{mod}}$ is the clear-sky modeled value of PAR(0^-) for the

same location and day as the measurement. The vertical profile of daily PAR(z) is finally modeled through the following equation:

$$\mathrm{PAR}(z) = \mathrm{PAR}(0^-)\exp(-K_d(\mathrm{PAR})\times z) \quad (5)$$

where K_d(PAR) (m^{-1}) is the diffuse attenuation coefficient for PAR; it is derived from equation (9) in *Morel et al.* [2007] that relates K_d(PAR) to the diffuse attenuation of downward irradiance at 490 nm, K_d(490), in a layer of thickness equal to $2\times[K_d(490)]^{-1}$:

$$K_d(\mathrm{PAR}) = 0.00665 + 0.874\times K_d(490) - 0.00121\times[K_d(490)]^{-1} \quad (6)$$

In equation (5) (and the rest of the study), K_d(PAR) is assumed to be constant in the euphotic zone. K_d(490) is derived from the noise-free $E_d(490, z, t_{noon})$ measurement.

The variables [Chl a](z), c_p(z), b_{bp}(z), PAR(z), PAR(0^-), and K_d(PAR) were interpolated every 10 days for the SPSG and NPSG floats and every 5 days for the NWMS and LS floats. Finally, we applied a three-point (SPSG and NPSG floats) and five-point (NWMS and LS floats) moving average to minimize the effect of mesoscale instabilities on the seasonal phytoplankton dynamics.

2.5. Variable Definition and Calculation

The different variables used in this study and their associated symbols, definitions, and units are detailed in Table 1.

The mixed layer depth (MLD) is defined as the depth where the density is greater than 0.03 kg m^{-3} with respect to its value at 10 m [*Montegut et al.*, 2004]. The MLD estimation was then interpolated every 10 days for the SPSG and NPSG floats and every 5 days for the NWMS and LS floats. Finally, we applied a three-point (SPSG and NPSG floats) and five-point (NWMS and LS floats) moving average.

Assuming that phytoplankton cells complete one revolution per day in the mixed layer during convective mixing [*D'Asaro*, 2008], the radiant energy they receive is the average value of the PAR(z) profile over the mixed layer, hereafter denoted as $\mathrm{PAR_{ML}}$ [*Morel et al.*, 2010]:

$$\mathrm{PAR_{ML}} = \frac{1}{\mathrm{MLD}}\int_{\mathrm{MLD}}^{0}\mathrm{PAR}(0^-)\exp(-K_d(\mathrm{PAR})\times z)\,dz \quad (7)$$

The first penetration depth, Z_{pd} (m), is defined as $1/K_d$(PAR) [*Gordon and McCluney*, 1975]. Note that this quantity is also used for ocean color remote sensing studies, where it delineates the surface layer that is seen by the satellite. The surface values of [Chl a], c_p, b_{bp}, c_p*, and b_{bp}* ($[\mathrm{Chl}]_{surf}$, c_{psurf}, b_{bpsurf}, c_{psurf}*, and b_{bpsurf}*) are calculated as the median within the first penetration depth.

Daytime nonphotochemical quenching (NPQ) at high irradiance [*Cullen and Lewis*, 1995] results in a decrease of the fluorescence emission (per unit of Chl a) when the phytoplankton cells are exposed to high oversaturating solar illumination. Such conditions are encountered within the upper layers of the ocean, especially during sunny days. As a result, the retrieval of $[\mathrm{Chl}]_{surf}$ acquired by in vivo fluorometers implemented on the Bio-Argo floats are expected to be systematically biased (depressed) at noon. $[\mathrm{Chl}]_{surf}$ estimates from Moderate Resolution Imaging Spectroradiometer (MODIS) sensor (unbiased by NPQ) are used to quantify the possible effect of NPQ on $[\mathrm{Chl}]_{surf}$ estimates from the floats. The 8 day level 3 composites in a 0.2°×0.2 box centered on the float location are used to provide match-up data. Figure S1 in the supporting information shows that for all floats, the consistency between floats and satellite values in terms of seasonal dynamics is rather good. In the LS and NWMS, there is also consistency in terms of amplitude. Here we do not attribute the underestimation of the in situ $[\mathrm{Chl}]_{surf}$ in the SPSG and NPSG compared to MODIS $[\mathrm{Chl}]_{surf}$ to the effect of NPQ. Instead, we preferentially attribute this underestimation to the calibration method, which possibly underestimates [Chl a] in such clear waters [*Xing et al.*, 2011]. Thus, the effect of NPQ seems to be relatively weak in our data set and does not require correction.

In the present study, we assume that in the open ocean (in particular in oligotrophic regions), the shape of the vertical profile of [Chl a] can be divided into two main types, Gaussian and sigmoid, similarly to *Mignot et al.* [2011]. The Gaussian shape is representative of phytoplankton living in a stratified environment, whereas the sigmoid shape is characteristic of phytoplankton homogeneously distributed in the mixing layer. The mixing (stratified) period is then defined as the period when the vertical profile of [Chl a] has a sigmoid (Gaussian) shape. The mixing period is highlighted by the stars in Figure 7.

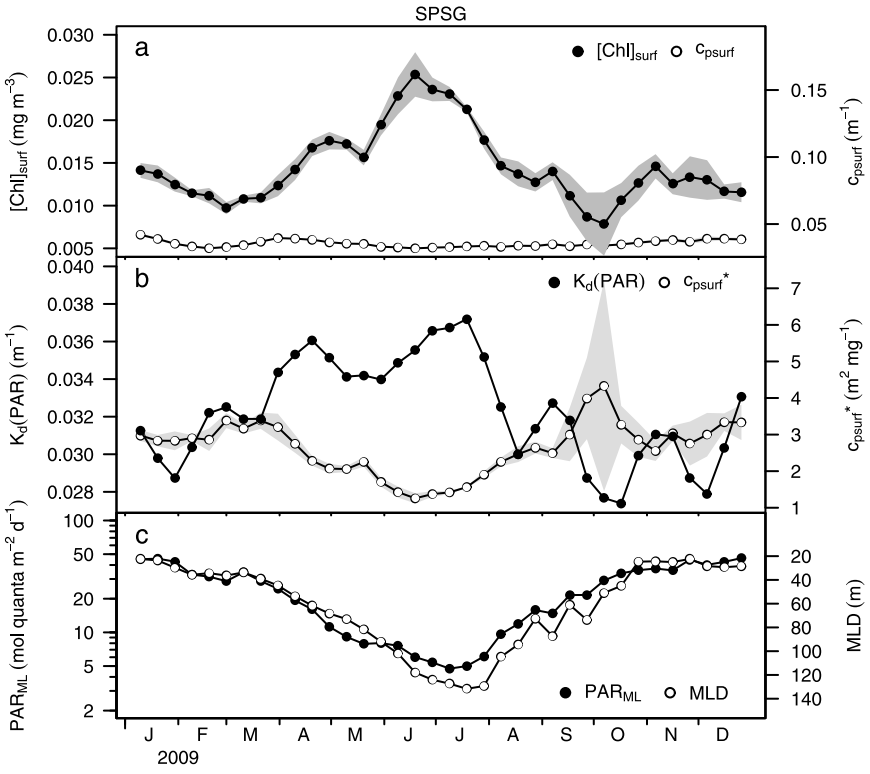

Figure 3. Illustration of the SPSG that includes the following: times series of the (a) median [Chl *a*] in the first penetration depth ($[Chl]_{surf}$, black circles, left axis) and median c_p in the first penetration depth (c_{psurf}, white circles, right axis), (b) diffuse attenuation coefficient (K_d(PAR), black circles, left axis) and ratio of (c_{psurf} to $[Chl]_{surf}$ (c_{psurf}*, white circles, right axis), and (c) average PAR in the mixed layer (PAR_{ML}, black circles, left axis) and mixed layer depth (MLD, white circles, right axis). Note that the scale of the *y* axis for c_{psurf} spans a similar dynamic range as for $[Chl]_{surf}$. The shaded areas are the standard deviations around the average cycle of $[Chl]_{surf}$ (dark gray shading), c_{psurf} (light gray shading), and c_{psurf} * (light gray shading).

To highlight the differences between spring, summer, and fall conditions, the data selection was performed for the first month (spring) and last month (fall) of the stratified period as well as for the month when the DCM was the deepest (summer). The SPSG was special compared to other systems, because the vertical profile of [Chl *a*] always had a Gaussian shape; therefore, the data selection for spring and fall could not be applied. The data collected 1 month after (spring) and 1 month before (fall) the date of the shallowest DCM were selected and utilized in our analysis. The symbols at the top of each panel in Figure 7 indicate the selected profiles (diamonds for the spring profiles, dots for the summer profiles, and triangles for the fall profiles).

When the vertical profile of [Chl *a*] has a Gaussian shape, the depth of the DCM (Z_{DCM}) is defined as the depth of the maximum [Chl *a*] ($[Chl]_{DCM}$). The values of c_p, b_{bp}, c_p*, b_{bp}*, and PAR at Z_{DCM} are hereafter denoted as c_{pDCM}, b_{bpDCM}, c_{pDCM}*, b_{bpDCM}*, and PAR_{DCM}. The yearly average PAR at the DCM is $\overline{PAR_{DCM}}$.

3. Results

In oligotrophic environments, the euphotic zone can be roughly considered as a two-layer system: (1) an upper mixed layer, which is a priori nutrient limited but not light limited, and (2) a deeper layer, which is a priori light limited, potentially less nutrient starved, and where the DCM develops. This conceptual scheme will be used in the following presentation and interpretation of the results.

3.1. The Upper Euphotic Mixed Layer

The time series of $[Chl]_{surf}$, c_{psurf} (or b_{bpsurf}), K_d(PAR), c_{psurf}* (or b_{bpsurf}*), PAR_{ML}, and MLD are shown for the four oligotrophic environments: SPSG (Figure 3), NPSG (Figure 4), LS (Figure 5), and NWMS (Figure 6). In the four oceanic studied regions, $[Chl]_{surf}$ and K_d(PAR) show maximum values during the winter mixing, whereas c_{psurf}* (or b_{bpsurf}*) reach a minimum in winter. In the NWMS, the simultaneous high values of $[Chl]_{surf}$ and K_d

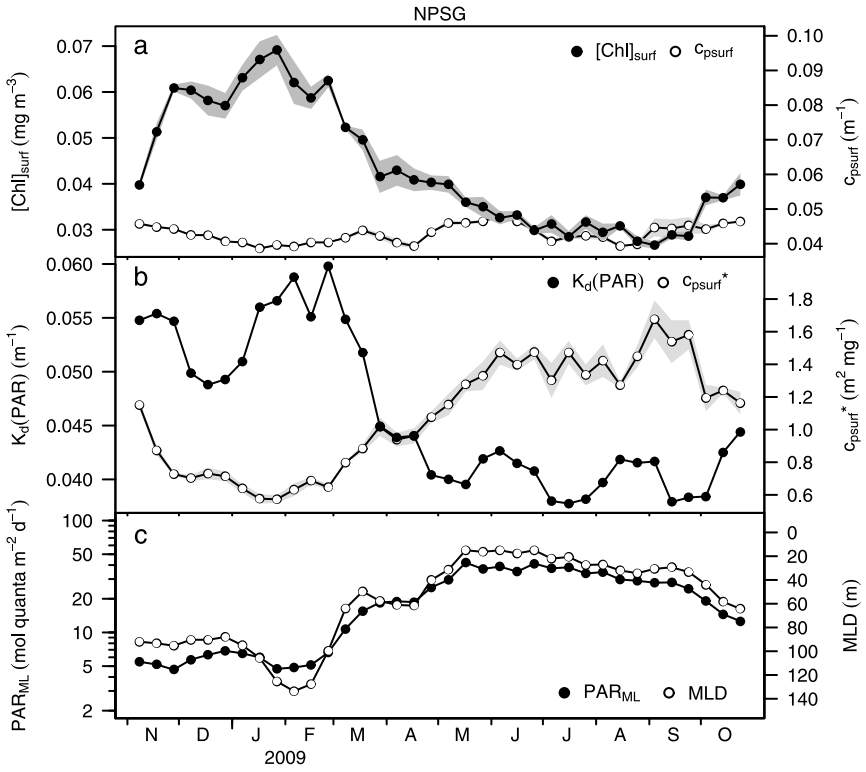

Figure 4. Same as in Figure 3 but for the NPSG.

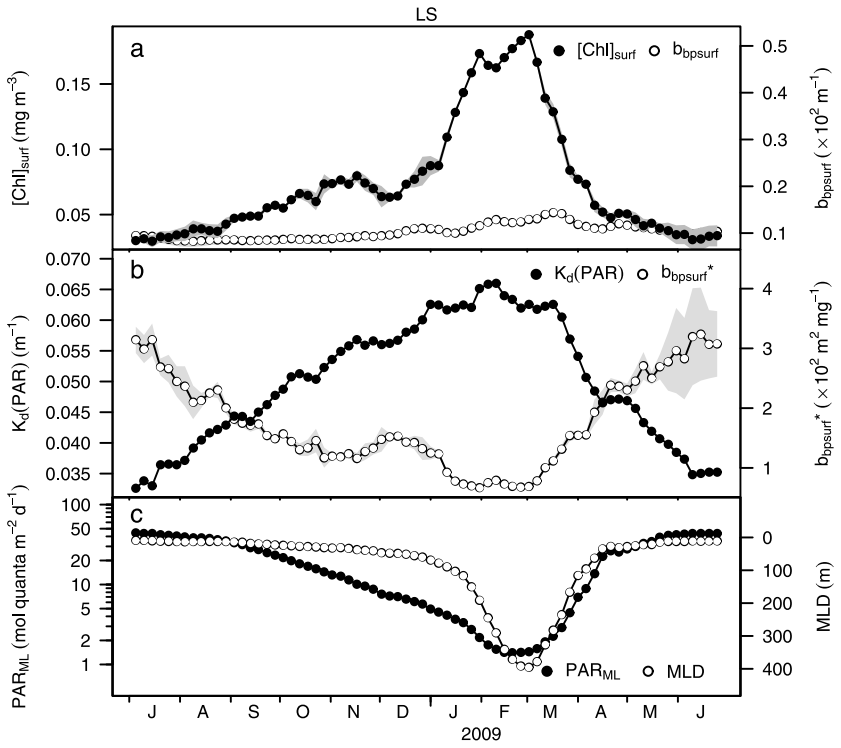

Figure 5. Same as in Figure 3 but for the LS.

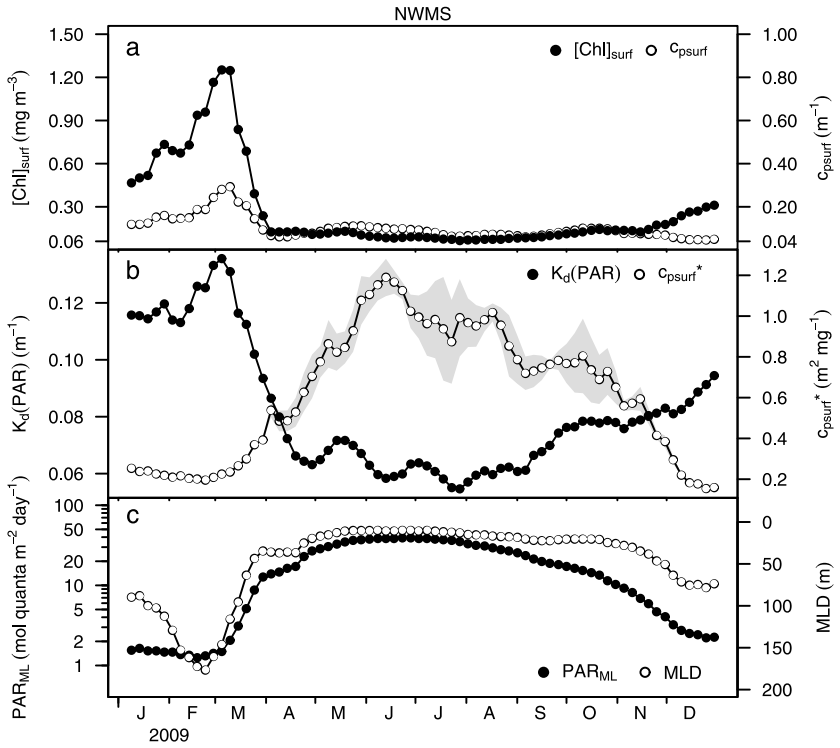

Figure 6. Same as in Figure 3 but for the NWMS.

(PAR) coincide with the maximum of c_{psurf} at the beginning of March 2009. In the LS, the b_{bpsurf} maximum occurs several weeks after $[Chl]_{surf}$ and K_d(PAR) reach their highest values. In the SPSG and NPSG, c_{psurf} is slightly lower during the winter mixing and remains relatively constant throughout the year.

Based on these results (Figures 3–6), it appears that in the oligotrophic ocean, the surface winter increase of [Chl *a*] is always associated with an increase in intracellular pigmentation. In the center of the subtropical gyres, the surface winter increase of [Chl *a*] is not associated with an increase of phytoplankton biomass, whereas in the Mediterranean Sea, the surface increase of [Chl *a*] is concomitant with an increase of phytoplankton biomass. This difference may be a result of the relative position of the mixed layer with respect to the depth of the nutrient pool.

In the four regions during the winter mixing, the average light intensity for phytoplankton in the mixed layer (PAR_{ML}) is strongly reduced with respect to summer conditions (up to a factor of about 10 for the SPSG and the NPSG and up to a factor of about 30 for the LS and NWMS; Figures 3c–6c) as a result of the concomitant action of the reduced surface light intensity and increased turbulence. To overcome this severe light limitation and minimize its influence on growth during the mixing period, phytoplankton respond with an increase of intracellular Chl *a* content [*Letelier et al.*, 1993; *Winn et al.*, 1995; *Morel et al.*, 2010].

In the center of the subtropical gyres, the mixed layer is not deep enough to reach the nutricline and subsequently injects autochthonous nutrients in the upper layer [*McClain et al.*, 2004]. Therefore, changes in intracellular pigment concentration fully account for the observed surface [Chl *a*] increase, and overall, phytoplankton biomass slightly decreases during the winter mixing (Figures 3a and 4a).

In the Mediterranean Sea, however, the simultaneous increase of [Chl *a*] and phytoplankton biomass (c_p or b_{bp}) observed in late winter is likely an indicator of typical bloom conditions in a nutrient-replete mixed layer (Figures 5a and 6a) [*D'Ortenzio and d' Alcala*, 2009]. However, the photoacclimation process still contributes to the surface increase of [Chl *a*], because the change in phytoplankton biomass accounts only for ~30% of the observed increase of [Chl *a*].

Satellite data earlier showed that [Chl *a*] variability in the surface mixed layer of the permanently stratified ocean reflects changes in intracellular pigment concentration rather than changes in phytoplankton carbon

biomass [*Behrenfeld et al*., 2005, 2008; *Siegel et al*., 2013]. The current study provides an independent, in situ validation of these earlier findings.

As expected, variations in $[Chl]_{surf}$ within the euphotic zone influence the diffuse attenuation coefficient for downwelling irradiance and therefore the amount of light available for phytoplankton growth in the layer below this upper layer. K_d(PAR) is maximum in winter when $[Chl]_{surf}$ is the highest. In the next section, we will discuss how this seasonal change in the surface layer K_d(PAR) influences the seasonal dynamics of phytoplankton in the lower euphotic-DCM layer.

3.2. The Lower Euphotic-DCM Layer

3.2.1. Depth of the DCM

In Figure 7, the temporal evolution of the [Chl *a*] distribution with depth is represented for each oceanic region under consideration in this study: Figure 7a, the SPSG; Figure 7b, the NPSG; Figure 7c, the LS; and Figure 7d, the NWMS. The black continuous line is the MLD, and the black dashed lines are the isolumes. For each oceanic region, the drawn isolumes comprise a range equivalent to approximately 1 standard deviation of $\overline{PAR_{DCM}}$ (SPSG, 0.1–0.4 mol quanta $m^{-2}\,d^{-1}$; NPSG, 0.1–0.6 mol quanta $m^{-2}\,d^{-1}$; LS, 0.1–0.6 mol quanta $m^{-2}\,d^{-1}$; and NWMS, 0.1–1.2 mol quanta $m^{-2}\,d^{-1}$).

The SPSG is characterized by a permanent DCM, whereas the DCM is destroyed in the three other regions when the mixed layer becomes deeper than $\overline{PAR_{DCM}}$ (i.e., during the mixing period; stars in Figure 7). Although the seasonal vertical displacement of the DCM ranges over different depths for the four oceanic areas, it nevertheless depicts a similar and generic pattern.

1. The DCM reaches its deepest position in summer (SPSG, January; NPSG, July; LS, July; and NWMS, July; dots in Figure 7).
2. The depth of the DCM decreases from summer to fall until the shallowest position is reached (triangles in Figure 7).
3. During the mixing period when the MLD becomes deeper than $\overline{PAR_{DCM}}$, the DCM is destroyed, and the vertical profile of [Chl *a*] shows a sigmoid-like shape (stars in Figure 7). This feature can be observed in all of the considered regions except the SPSG, where the DCM is never destroyed and remains at its shallowest position when the mixed layer is the deepest. In this particular case, the MLD never reaches the depth of $\overline{PAR_{DCM}}$.
4. In spring (diamonds in Figure 7), the restratification of the water column enables the progressive formation of the DCM, which is located at a similar depth as in fall.
5. The DCM deepens from spring to summer.

In the four studied regions, the seasonal variation of the isolumes depicts the same displacement as the depth of the DCM, which is shallower in spring and fall and deeper in summer. The DCM depth displacement appears to be light driven in the four regions, as reported by LTL04 in the NPSG.

Figure 8 shows the annual (black curve) and seasonal (colored curves) average vertical distributions of [Chl *a*] as a function of PAR. LTL04 showed that in the NPSG, the DCM follows a fixed isolume throughout the year (i.e., 0.5 mol quanta $m^{-2}\,d^{-1}$; horizontal dashed line in Figure 8). However, our observations suggest that the DCM is located at a different isolume for each season.

The seasonal DCM depth dynamics result from a light-driven low-frequency process on which higher-frequency fluctuations can be superimposed. At short time scales of several days, the DCM is tightly linked to a specific isopycnal [*Dandonneau and Lemasson*, 1987; *Claustre et al*., 1999], and any short-term vertical displacement of isopycnals results in a displacement of the DCM with respect to the average value of PAR_{DCM} ($\overline{PAR_{DCM}}$). These short-term isopycnal fluctuations are caused by tidal and near-inertial oscillations and range between −30 m and +30 m [*Letelier et al*., 1993]. Compared to the study of LTL04, the float sampling strategy adopted here (one upward cast every 5 or 10 days) does not correct for the effects of tidal and near-inertial oscillations. Therefore, the seasonal discrepancies in PAR_{DCM} observed here could be attributed to the higher-frequency displacements in the DCM depth. Similarly, LTL04 suggested that the position of the DCM is influenced by fluctuations in the light field during the several days prior to measurement. Hence, because of short time scale changes in the cloud coverage, the actual position of the DCM may deviate significantly from the position estimated from the cloud coverage and light field at the time of the measurements.

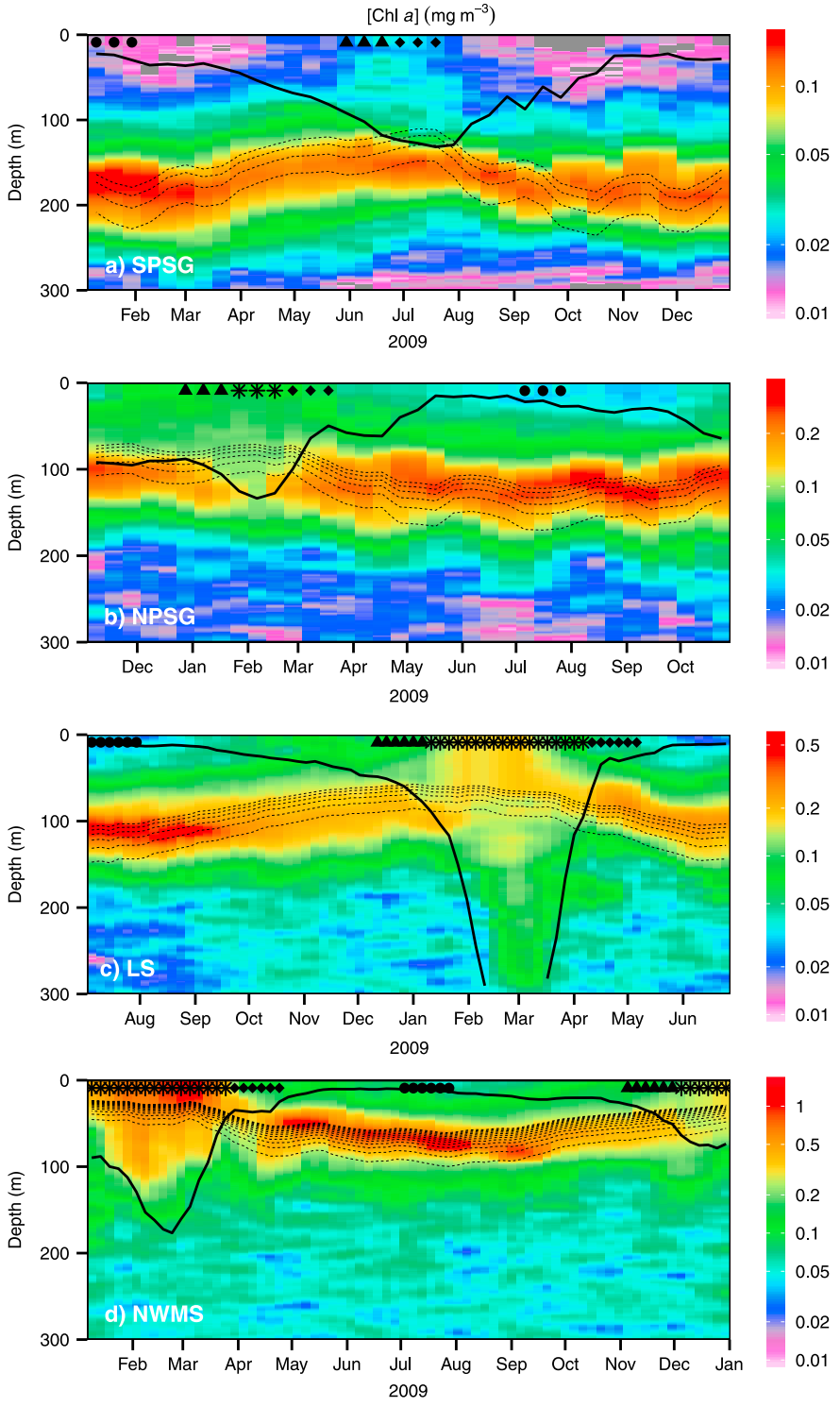

Figure 7. Time series of the 0–300 m vertical distribution of [Chl *a*] for (a) SPSG, (b) NPSG, (c) LS, and (d) NWMS. The solid black line is the mixed layer depth (MLD). The black dashed lines are the isolumes. For each oceanic region, the isolumes are within a range equivalent to the yearly average light at the DCM ($\overline{PAR_{DCM}}$), which is approximately 1 standard deviation (SPSG: 0.1–0.4 mol quanta m^{-2} d^{-1}, NPSG: 0.1–0.6 mol quanta m^{-2} d^{-1}, LS: 0.1–0.6 mol quanta m^{-2} d^{-1}, and NWMS: 0.1–1.2 mol quanta m^{-2} d^{-1}). The symbols at the top of each panel indicate the profiles that have been used to compute the seasonal average profiles displayed in Figures 8 and 10 (diamond for the spring profiles, dots for the summer profiles, and triangles for the fall profiles). The stars represent the profiles during the mixing period.

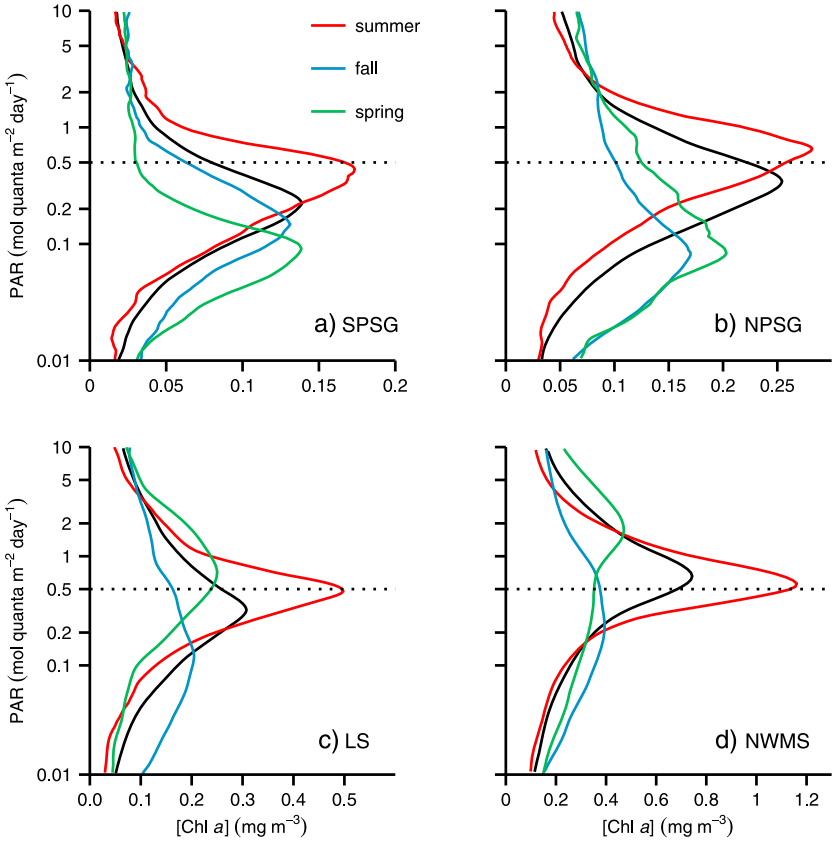

Figure 8. Vertical distribution of [Chl *a*] as a function of PAR for the four oligotrophic regions and over different time periods: (a) SPSG, (b) NPSG, (c) LS, and (d) NWMS. The dashed line corresponds to the 0.5 mol quanta $m^{-2} d^{-1}$ isolume.

On a yearly basis, the absolute value of light at the DCM differs slightly between oceanic regions (black line in Figure 8). The lowest value is found in the SPSG (mean = 0.22 mol quanta $m^{-2} d^{-1}$, SD = 0.12 mol quanta $m^{-2} d^{-1}$, and $n = 36$). The LS and the NPSG have a similar intermediate value (NPSG, mean = 0.34 mol quanta $m^{-2} d^{-1}$, SD = 0.23 mol quanta $m^{-2} d^{-1}$, and $n = 33$ and LS, mean = 0.32 mol quanta $m^{-2} d^{-1}$, SD = 0.23 mol quanta $m^{-2} d^{-1}$, and $n = 53$). Finally, the highest value is found in the NWMS (mean = 0.66 mol quanta $m^{-2} d^{-1}$, SD = 0.54 mol quanta $m^{-2} d^{-1}$, and $n = 51$). Therefore, the DCM becomes shallower relative to the light intensity from blue (SPSG) to green (NWMS) waters, which suggests that the spectral quality of light may affect the position of the DCM with respect to isolumes.

Because of the limited set of wavelengths at which irradiance is measured by the Bio-Argo float, the impact of spectral changes in irradiance with depth on the DCM location is tentative. Nevertheless, in clear (and stable) waters associated with "deep" DCMs, such as in the SPSG, which is the end member of such systems [*Claustre et al.*, 2008], photosynthetic organisms like *Prochlorococcus* [*Ras et al.*, 2008] have adapted their pigment composition (e.g., divinyl chlorophyll *a* and divinyl chlorophyll *b*) to match and take advantage of the spectral quality of available photons. As a consequence, for a given PAR at the DCM, deeper DCMs benefit from larger photosynthetically usable radiation (the convolution of PAR with photosynthetic absorption [e.g., *Morel et al.*, 1987]) than shallower DCMs. In other words, phytoplankton and especially *Prochlorococcus* at a deep DCM can accommodate lower PAR levels, because they are more efficient at capturing the remaining blue photons. Evidence for this adaptation may be observed in the decreasing yearly average isolume according to the increasing yearly average DCM depth (see Figure 12c).

In the following sections, we assume that the seasonal depth displacements of the DCM are light driven and tightly linked to a unique absolute value of irradiance ($\overline{PAR_{DCM}}$) regardless of the season. Thus, following the

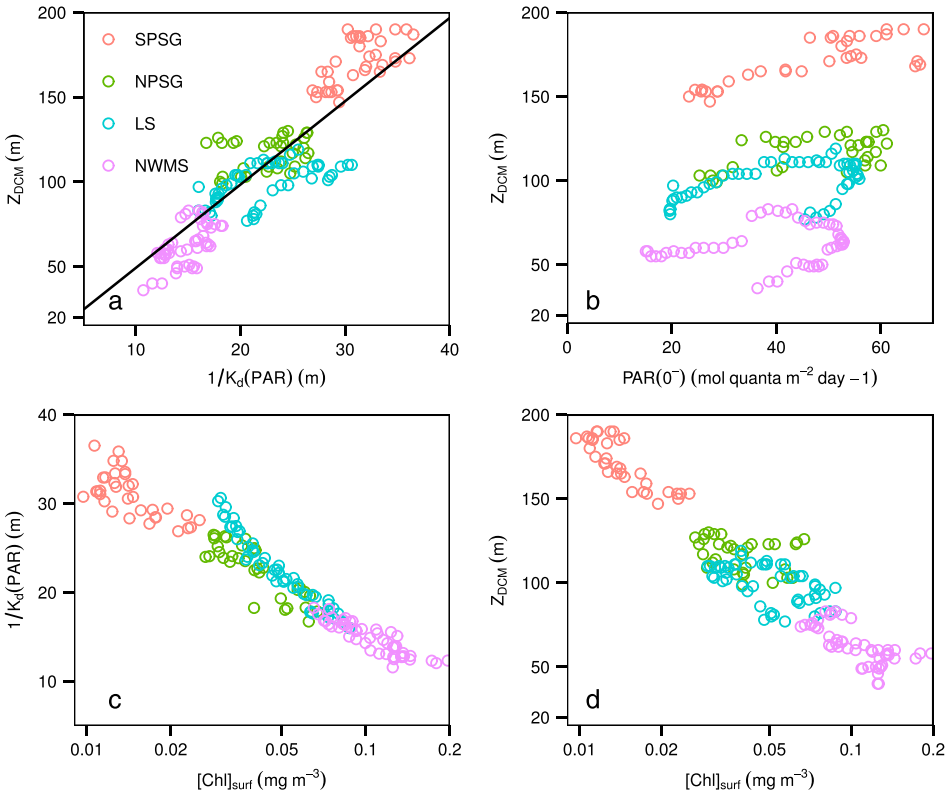

Figure 9. Relationship between various descriptors of oligotrophic regimes during the stratified period. (a) Scatterplot of the depth of the DCM Z_{DCM} (m) as a function of the inverse of the diffuse attenuation coefficient of PAR $1/K_d$(PAR) (m) according the oceanic regions. The black line represents the relationship $Z_{DCM} = 4.92 \cdot 1/K_d(\mathrm{PAR})$. (b) Scatterplot of Z_{DCM} (m) as a function of PAR under the sea surface PAR(0^-) (mol quanta $m^{-2}\,d^{-1}$) according the oceanic regions. (c) Scatterplot of $1/K_d$(PAR) (m) as a function of the median [Chl *a*] in the first 40 m $[Chl]_{surf}$ (mg m^{-3}) according the oceanic regions. (d) Scatterplot of Z_{DCM} (m) as a function of $[Chl]_{surf}$ (mg m^{-3}) according the oceanic regions.

Beer–Lambert law, the depth of the DCM, Z_{DCM}, can be expressed as a function of PAR under the sea surface, PAR(0^-), and diffuse attenuation coefficient, K_d(PAR), which is considered constant with depth:

$$Z_{DCM} = -\log\left[\overline{\mathrm{PAR}_{DCM}} \,/\, \mathrm{PAR}(0^-)\right] / K_d(\mathrm{PAR}) \tag{8}$$

Therefore, the depth of the DCM is correlated with $1/K_d$(PAR) and PAR(0^-) (i.e., Z_{DCM} increases when K_d(PAR) decreases and PAR(0^-) increases and vice versa). However, variations in Z_{DCM} appear to be more sensitive to K_d(PAR) than to PAR(0^-), because the incident flux has a logarithm impact on the DCM depth, whereas a change in attenuation has a linear impact. For a constant $\overline{\mathrm{PAR}_{DCM}}$ of 0.35 mol quanta $m^{-2}\,d^{-1}$ and K_d(PAR) of 0.045 m^{-1}, a 50% increase in PAR(0^-) results in a deepening of the DCM by ~9%. Inversely, assuming PAR(0^-) = 45 mol quanta $m^{-2}\,d^{-1}$, a 50% decrease in K_d(PAR) results in a deepening of the DCM by ~100%.

Figures 9a and 9b show the relationship between Z_{DCM} and $1/K_d$(PAR) and between Z_{DCM} and PAR(0^-). As expected from equation (8), Z_{DCM} deepens as K_d(PAR) decreases (Figure 9a) and PAR(0^-) increases (Figure 9b), although this latter relationship is considerably weaker. For a similar value of PAR(0^-) among the four basins, different values of Z_{DCM} are found (Figure 9b), whereas there is a unique common slope (in the first approximation) linking Z_{DCM} and $1/K_d$(PAR) among the four regions, which indicates a linear regression through the origin (black line in Figure 9a):

$$Z_{DCM} = 4.92\,/K_d(\mathrm{PAR}),\ p < 0.001,\ n = 173. \tag{9}$$

If the assumption that the DCM is tightly linked to a unique isolume regardless of the season is relaxed in equation (8), then equation (9) suggests that the DCM lies on a fixed percent isolume independent of basin and season (i.e., $\mathrm{PAR}_{DCM} = 0.73\%\,\mathrm{PAR}(0^-)$]. In this case, no variability in the relationship between Z_{DCM}

and $1/K_d$(PAR) should be observed, and the DCM layer should coincide with a higher light intensity in summer compared to spring and fall. However, in the LS and NWMS, the DCM is located at a higher light intensity in spring (Figures 8c and 8d). Moreover, there is a significant variability in each oceanic region between Z_{DCM} and $1/K_d$(PAR) (Figure 9a), even if this variability could also be attributed to short-term displacements of the DCM regardless of the isolume position (as mentioned above). For those reasons, we consider equation (9) to be representative of yearly average conditions: $\log\left[\overline{PAR_{DCM}}/\overline{PAR(0^-)}\right] = -4.92$, where $\overline{PAR(0^-)}$ is the yearly average PAR(0^-). Considering a similar $\overline{PAR(0^-)} = 45$ mol quanta $m^{-2}\,d^{-1}$ value for the four oceanic regions, an estimation of $\overline{PAR_{DCM}} \sim 0.33$ mol quanta $m^{-2}\,d^{-1}$ can be derived. This estimation is close to the $\overline{PAR_{DCM}}$ values found in the LS and NPSG (Figure 8). Note that in the SPSG and NWMS (Figure 9a), data show higher and lower values compared to the relationship of generic Z_{DCM} to $1/K_d$(PAR) (black line). The slopes linking Z_{DCM} and $1/K_d$(PAR) are then 5.46 ($p < 0.001$, $n = 36$) and 4.21 ($p < 0.001$, $n = 51$), which leads to a $\overline{PAR_{DCM}}$ of ~0.19 and 0.67 mol quanta $m^{-2}\,d^{-1}$, which is consistent with the observed values (Figure 8).

At this stage, it should be remembered that K_d(PAR) is derived from the diffuse attenuation coefficient for downward irradiance at 490 nm, K_d(490), at a depth equivalent to 2 times the first penetration depth (see also equation (6)). In case 1 waters, there is a direct link between the attenuation coefficient K_d and [Chl *a*] [*Morel*, 1988; *Morel and Maritorena*, 2001], which is clearly highlighted in Figure 9c. Hence, as expected, the depth of the DCM is inversely related to $[Chl]_{surf}$ (Figure 9d), an observation that was previously made by *Mignot et al.* [2011] for the global ocean.

3.2.2. Magnitude of the DCM

The conceptual analysis of LTL04 is based on the comparison of the average vertical profile of [Chl *a*] between winter and summer. In their study, a DCM was present during winter, which is not the case for the current observations (except in the SPSG). We apply the same methodology as LTL04 except that we compared the average vertical profiles of [Chl *a*], c_p, and c_p*([Chl *a*], b_{bp}, and b_{bp}* for the LS) of spring, summer, and fall (Figure 10). Because the depth of the DCM is different throughout the seasons, the seasonal average profiles are represented according to an adjusted depth (i.e., the actual depth minus the depth of the DCM [*Hense and Beckmann*, 2008]). The seasonal average of [Chl *a*], c_p, and c_p*([Chl *a*], b_{bp}, and b_{bp}* for the LS) at the DCM was compared using a Student's *t* test (level of significance $p = 0.05$).

In the four oceanic regions and for each season, c_p* or b_{bp}* always reaches a minimum at the depth of the DCM (adjusted depth = 0). At the DCM, we observe a statistically significant increase in $[Chl]_{DCM}$ from spring to summer and a decrease from summer to fall (Figures 10a, 10d, 10g, and 10j; [Chl *a*] at adjusted depth = 0). The spring values are not statistically different from the fall values for the SPSG, NPSG, and NWMS. Spring values are greater than fall values for the LS. Similar statistically significant patterns are recorded in the c_p (or b_{bp} in the LS) signal at the DCM for the four oceanic regions (Figures 10b, 10e, 10h, and 10k; c_p (or b_{bp} in the LS) at an adjusted depth = 0) except that c_{pDCM} is higher in spring compared to fall in the SPSG, NPSG, and LS. In addition, c_{pDCM}* (b_{bpDCM}* in the LS) is not significantly different between seasons for the four oceanic regions (Table 2 and Figures 10c, 10f, 10i, and 10k; c_{pDCM}* (or b_{bpDCM}* in the LS) at adjusted depth = 0) except in the LS and NPSG, where c_{pDCM}* is significantly lower during summer (Figures 10f and 10l). Finally, for the four oceanic regions investigated here, the summer c_p (b_{bp}) profiles present a pronounced maximum at the depth of the DCM (DBM). This DBM is also evident during springtime in the LS.

Based on these observations, it appears that the presence of a deep chlorophyll maximum in oligotrophic regions always results from a photoacclimation process. In each of the regions investigated in this study, the [Chl *a*] at the DCM increases from spring to summer and then decreases from summer to fall. The simultaneous seasonal variations of $[Chl]_{DCM}$ and c_{pDCM} (b_{bpDCM} in the LS) and the stability of c_{pDCM}* (b_{bpDCM}* in the LS) over the seasons indicate that [Chl *a*] variations in the lower euphotic zone result from biomass variations and not from photoacclimation processes. Therefore, in summer, in addition to the photoacclimation effect on [Chl *a*], the DCM also results from a change in biomass. Furthermore, the stability of c_{pDCM}* (b_{bpDCM}* in the LS) over the seasons supports the observations of LTL04, who indicated that the amount of photons reaching the depth of the DCM remains constant during the year. This result implies that the accumulation of phytoplankton biomass from spring to summer is not triggered by a change in the light level but by an increase in the nutrient concentration in the lower euphotic zone. Indeed, the pool of nutrients present at depth becomes available to phytoplankton only when the isolumes start deepening from spring to summer [*Letelier et al.*, 2004]. Yet the nutrient supply stimulates phytoplankton growth, which might initiate a decoupling between the

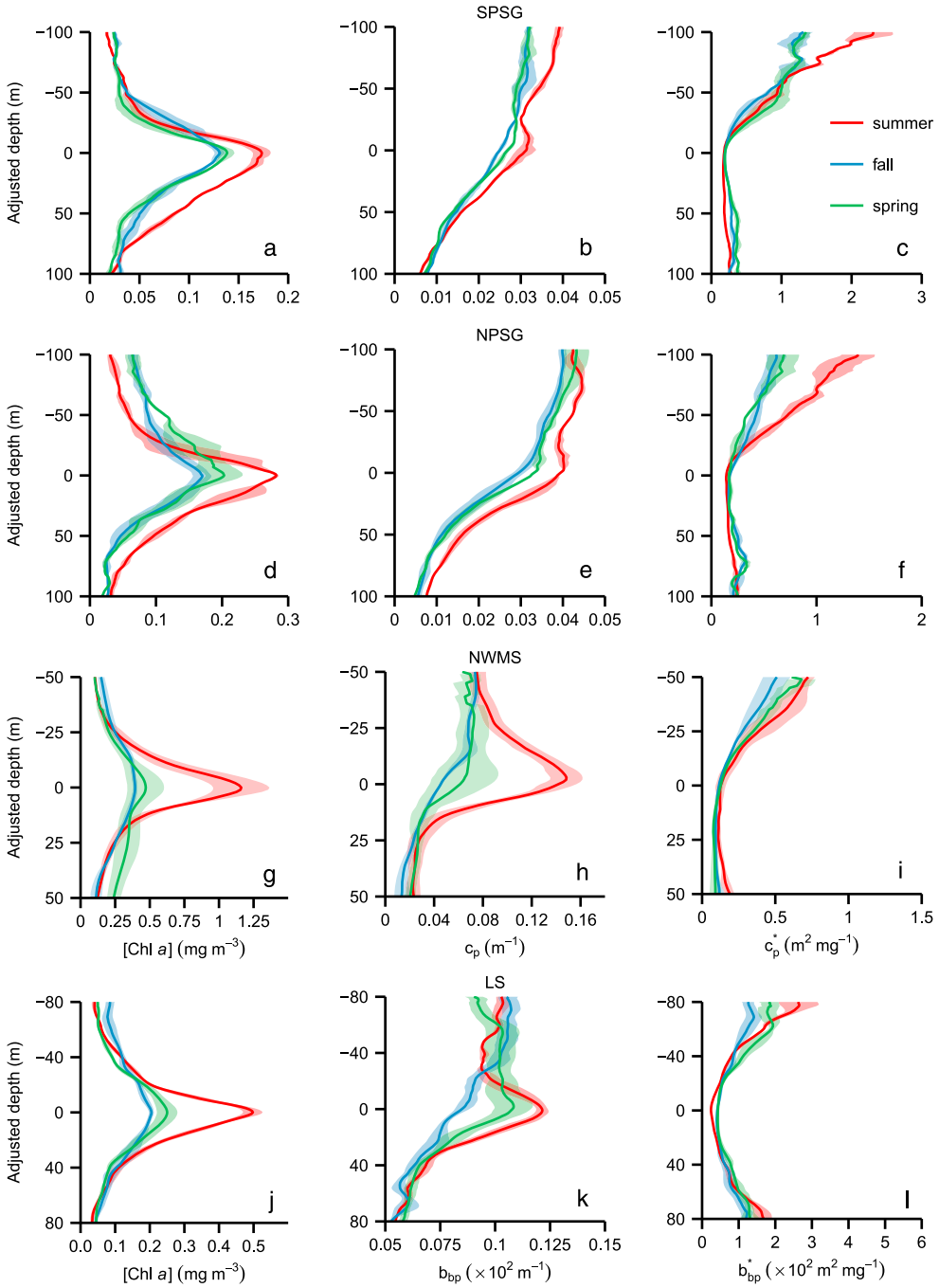

Figure 10. Comparison of the average depth distribution of [Chl *a*] (mg m^{-3}), c_p (b_{bp} in the LS) (m^{-1}), and ratio c_p* (b_{bp}* in the LS) (m^2 mg^{-1}) for spring (green line), summer (red line), and fall (blue line) for the (a–c) SPSG, (d–f) NPSG, (g–i) NWMS, and (j–l) LS. The adjusted depth (i.e., depth normalized by the depth of the DCM [*Hense and Beckmann*, 2008]) has been selected to account for the vertical displacements of the DCM between spring, summer, and fall. The colored shading represents the standard deviations around the corresponding seasonal average profiles.

phytoplankton division and loss (grazing) rate and cause the phytoplankton biomass to accumulate. Since the grazing losses are proportional to the concentration of food (biomass) [*Behrenfeld and Boss*, 2014], the biomass continues to accumulate (i.e., from spring to summer) as long as the rate of phytoplankton division is increasing. The equilibrium between the grazing losses and division rate is reestablished when the isolumes stop deepening in summer (Figure 7). Finally, when isolumes start shoaling in fall, the nutrients become progressively

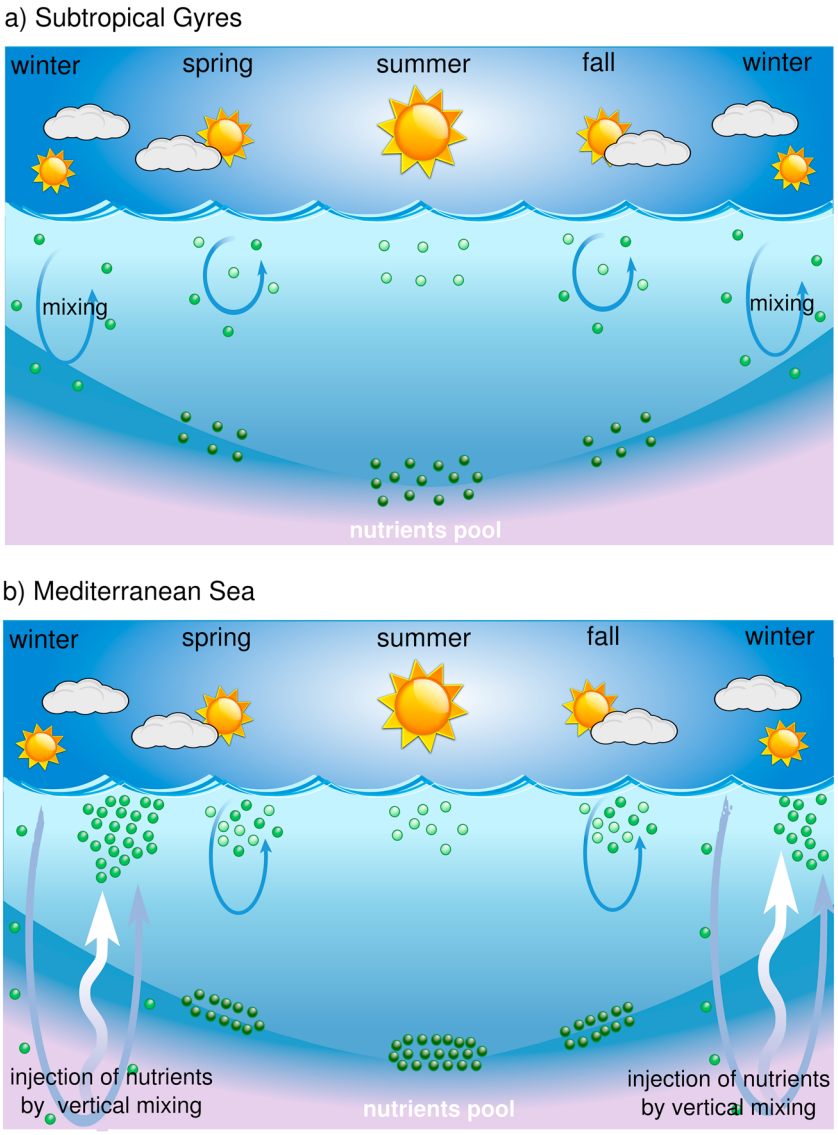

Figure 11. Conceptual scheme of the dynamics of phytoplankton that assumes a two-layer euphotic zone in (a) the subtropical gyres and (b) the Mediterranean Sea.

out of reach for the phytoplankton. This nutrient depletion causes phytoplankton biomass to further decrease because the phytoplankton cell division rate becomes lower than the grazing loss rate. In this depth horizon, the phototrophic production of organic matter from spring to summer corresponds to new primary production. Therefore, the formation of a DBM can be considered as clear evidence of new production occurring at the DCM.

4. Conclusion

Before the use of bio-optical profiling floats, studies of the seasonal dynamics of phytoplankton biomass in oligotrophic environments occurred at permanent oceanic stations or were based on ocean color satellite imagery. Although fixed oceanic stations perform in situ biogeochemical measurements within the euphotic zone with sparse repetitive sampling, satellite remote sensing platforms only sample the upper part of the euphotic zone. Therefore, large uncertainties remain in the seasonal behavior of oligotrophic phytoplankton communities. In contrast, Bio-Argo floats offer the invaluable advantage of documenting the deep seasonal dynamics of biogeochemical properties with a high sampling frequency (5–10 days) over relatively long periods of time (1–2 years) in remote oceanic regions. Our bio-optical profiling floats

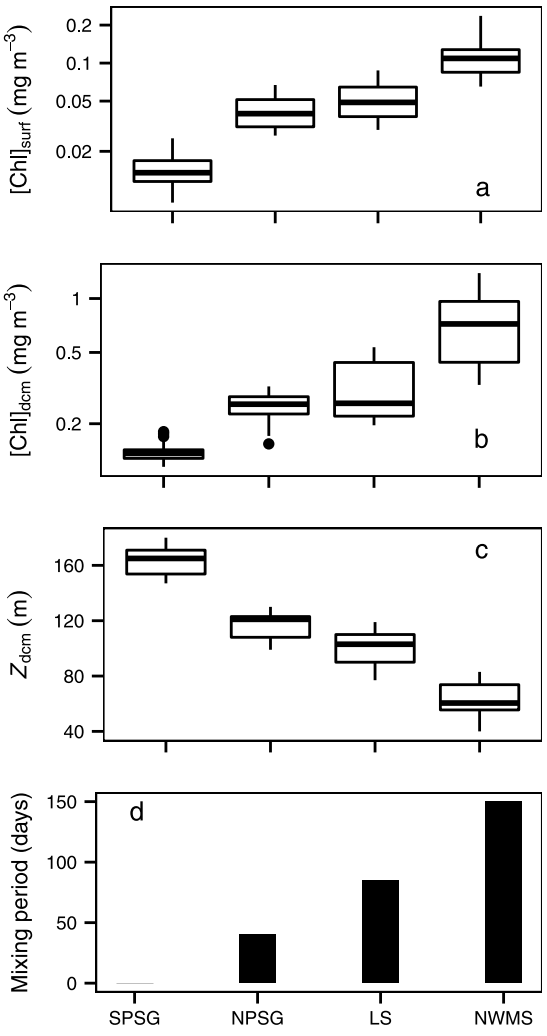

Figure 12. Boxplot of the average (a) [Chl *a*] in the first penetration depth $[Chl]_{surf}$, (b) [Chl *a*] at the DCM $[Chl]_{DCM}$, (c) depth of the DCM (Z_{DCM}) during the stratified period, and (d) mixing period (expressed in days) for the four oceanic regions.

deployed in four oligotrophic environments have provided a unique set of physical and bio-optical data that allowed studying the seasonal dynamics of phytoplankton in a holistic manner.

A common mechanism drives the seasonal pattern of phytoplankton biomass in the euphotic layer independent of the considered region. Figure 11 proposes a conceptual view of this mechanism. In the lower part of the euphotic layer, the seasonal displacement of the DCM is light driven. During winter, [Chl *a*] increases in the upper euphotic mixed layer as a result of photoacclimation (Figures 11a and 11b). In the Mediterranean Sea (Figure 11b), the [Chl *a*] increase is also associated with an increase in biomass that results from nutrient injection. The high surface Chl *a* concentration results in a light attenuation increase from fall to spring. Consequently, the isolumes and depth of the DCM become shallower. However, from spring to summer, when the [Chl *a*] in the upper part decreases along with the decrease in light attenuation, the DCM deepens and becomes closer and sometimes reaches the nitracline. This results in an enhancement of phytoplankton biomass at the DCM.

Although the same seasonal dynamics are observed in the four studied oligotrophic regions, there is a clear regional gradient in the characteristics of the phytoplankton vertical distribution, which is revealed by $[Chl]_{surf}$, $[Chl]_{DCM}$, and Z_{DCM}. For each region considered in our analysis, Figure 12 presents the boxplot of the stratified period: Figure 12a = $[Chl]_{surf}$, Figure 12b = $[Chl]_{DCM}$, Figure 12c = Z_{DCM}, and Figure 12d = the mixing period (i.e., the period when the vertical profile of [Chl *a*] has a sigmoid shape). The SPSG is considered as the end-member of the oligotrophic ocean [*Claustre and Maritorena*, 2003; *Claustre et al*., 2008] and shows the lowest values of $[Chl]_{surf}$ and $[Chl]_{DCM}$ as well as the deepest Z_{DCM}. These quantities then increase (decrease for Z_{DCM}) from the SPSG to the NPSG, LS, and NWMS. This gradient is closely related to the mixing period, which is null in the SPSG and the longest in the NWMS (~150 days). Thus, the duration (and intensity) of the winter mixing acts as a seasonal reset of the oligotrophic conditions. In the SPSG where this reset does not occur (at least for the year examined in this study), the observed pattern is essentially governed by the annual cycle of surface irradiance and MLD and representative of a steady state system. In the NWMS, however, the duration and intensity of the winter mixing allow a significant amount of nutrient availability for the growing season. Nutrient exhaustion arrives relatively later in the season and delays the progressive establishment of oligotrophic conditions, which are restricted to a shorter period.

This analysis considers the ecosystem from a "bottom-up" perspective. We focus only on resources regulating phytoplankton growth (light and nutrients) rather than factors influencing losses. Moreover, the role of nutrients is investigated indirectly by examining the dynamics of MLD and therefore remains to be confirmed. Further investigations using bio-optical floats equipped with nitrate sensors [*Johnson et al*., 2010] are required to properly assess the role of nutrients in this mechanism. Additionally, the role of grazers (top-down control)

should also be considered, because they are known to be responsible for the decline of phytoplankton biomass in the lower euphotic-DCM layer from summer to fall.

In this study, we present an analysis of continuous 1 year time series acquired by four floats. Restricting our analysis to a single year limits the possibility of developing a solid statistical assessment of the uncertainties that may bias the described seasonal patterns. Even if the reproducibility of seasonal patterns in the four distinct regions provides some level of confidence to our interpretation, future studies should clearly consider data sets acquired over longer time periods (several consecutive years). Similarly, the sampling strategy adopted here was not optimal for examining the seasonal dependency of the DCM to one particular isolume. New missions should be considered to properly assess this specific question using Bio-Argo floats.

In general, phytoplankton blooms occurring in the upper euphotic mixed layer of the temperate and subpolar ocean are considered to be important drivers of the ocean carbon uptake and marine food chain. Because of the absence of phytoplankton blooms in the upper euphotic mixed layer of the central part of the subtropical gyres, these remote ecosystems have long been considered to support exclusively regenerated production with limited export of carbon. In contrast, our observations suggest that new production occurs from spring to summer in the lower part of the euphotic layer (~150–200 m) of these systems. Even if this deep production is significantly lower than that supported by upper layer phytoplankton blooms, it may still be sufficient to sustain upper trophic levels and the export of organic matter. Finally, the evidence of a common phytoplankton biomass seasonal pattern in four distinct remote oceanic regions is remarkable and suggests that a similar mechanism might operate in all of the oligotrophic areas of the ocean where a DCM forms, which accounts for 50% of the global ocean.

Acknowledgments

This paper represents a contribution to the remOcean project, which is funded by the European Research Council (grant agreement 246777) and the Plateformes Autonomes et Biogeochimie Oceanique project, which is funded by Agence Nationale de la Recherche. We express our gratitude to Bernard Gentili for his help in the programming. We also thank the crew of the various cruises who deployed the Bio-Argo floats used in the present study. The authors also acknowledge the valuable comments and suggestions made by Ricardo Letelier and Michael Behrenfeld. Alexandre Mignot was funded through a grant provided by the French space agency "Centre National d'Etude Spatiale" and the French research institute for exploration of the sea "Institut Francais de Recherche pour l'Exploitation de la Mer."

References

Antoine, D., J. M. Andre, and A. Morel (1996), Oceanic primary production 2. Estimation at global scale from satellite (coastal zone color scanner) chlorophyll, *Global Biogeochem. Cycles*, *10*(1), 57–69, doi:10.1029/95GB02832.

Behrenfeld, M. J., and E. Boss (2003), The beam attenuation to chlorophyll ratio: An optical index of phytoplankton physiology in the surface ocean?, *Deep-Sea Res. Part I -Oceanogr. Res. Pap.*, *50*(12), 1537–1549, doi:10.1016/j.dsr.2003.09.002.

Behrenfeld, M. J., and E. Boss (2006), Beam attenuation and chlorophyll concentration as alternative optical indices of phytoplankton biomass, *J. Mar. Res.*, *64*(3), 431–451, doi:10.1357/002224006778189563.

Behrenfeld, M. J., and E. S. Boss (2014), Resurrecting the ecological underpinnings of ocean plankton blooms, in *Annual Review of Marine Science*, vol. 6, edited by C. A. Carlson and S. J. Giovannoni, pp. 167–U208, Annual Reviews, Palo Alto, Calif.

Behrenfeld, M. J., E. Boss, D. A. Siegel, and D. M. Shea (2005), Carbon-based ocean productivity and phytoplankton physiology from space, *Global Biogeochem. Cycles*, *19*, GB1006, doi:10.1029/2004GB00229.

Behrenfeld, M. J., R. T. O'Malley, D. A. Siegel, C. R. McClain, J. L. Sarmiento, G. C. Feldman, A. J. Milligan, P. G. Falkowski, R. M. Letelier, and E. S. Boss (2006), Climate-driven trends in contemporary ocean productivity, *Nature*, *444*(7120), 752–755, doi:10.1038/nature05317.

Behrenfeld, M. J., K. H. Halsey, and A. J. Milligan (2008), Evolved physiological responses of phytoplankton to their integrated growth environment, *Philos. Trans. R. Soc. B-Biol. Sci.*, *363*(1504), 2687–2703, doi:10.1098/rstb.2008.0019.

Bishop, J. K. B. (1999), Transmissometer measurement of POC, *Deep-Sea Res. Part I -Oceanogr. Res. Pap.*, *46*(2), 353–369, doi:10.1016/S0967-0637(98)00069-7.

Bishop, J. K. B., and T. J. Wood (2009), Year-round observations of carbon biomass and flux variability in the Southern Ocean, *Global Biogeochem. Cycles*, *23*, GB2019, doi:10.1029/2008GB003206.

Bosc, E., A. Bricaud, and D. Antoine (2004), Seasonal and interannual variability in algal biomass and primary production in the Mediterranean Sea, as derived from 4 years of SeaWiFS observations, *Global Biogeochem. Cycles*, *18*, GB1005, doi:10.1029/2003GB002034.

Boss, E., and W. S. Pegau (2001), Relationship of light scattering at an angle in the backward direction to the backscattering coefficient, *Appl. Opt.*, *40*(30), 5503–5507, doi:10.1364/AO.40.005503.

Bricaud, A., A. Morel, and L. Prieur (1981), Absorption by dissolved organic-matter of the sea (yellow substance) in the UV and visible domains, *Limnol. Oceanogr.*, *26*(1), 43–53.

Cetinic, I., M. J. Perry, N. T. Briggs, E. Kallin, E. A. D'Asaro, and C. M. Lee (2012), Particulate organic carbon and inherent optical properties during 2008 North Atlantic Bloom Experiment, *J. Geophys. Res.*, *117*, C06028, doi:10.1029/2011JC007771.

Claustre, H., and S. Maritorena (2003), The many shades of ocean blue, *Science*, *302*(5650), 1514–1515, doi:10.1126/science.1092704.

Claustre, H., A. Morel, M. Babin, C. Cailliau, D. Marie, J. C. Marty, D. Tailliez, and D. Vaulot (1999), Variability in particle attenuation and chlorophyll fluorescence in the tropical Pacific: Scales, patterns, and biogeochemical implications, *J. Geophys. Res.*, *104*(C2), 3401–3422, doi:10.1029/98JC01334.

Claustre, H., A. Sciandra, and D. Vaulot (2008), Introduction to the special section bio-optical and biogeochemical conditions in the South East Pacific in late 2004: The BIOSOPE program, *Biogeosciences*, *5*(3), 679–691.

Coale, K., and K. Bruland (1987), Oceanic stratified euphotic zone as elucidated by Th-234-U-238 disequilibria, *Limnol. Oceanogr.*, *32*(1), 189–200.

Cullen, J. (1982), The deep chlorophyll maximum: Comparing vertical profiles of chlorophyll-A, *Can. J. Fish. Aquat. Sci.*, *39*(5), 791–803, doi:10.1139/f82-108.

Cullen, J., and M. Lewis (1995), Biological processes and optical measurements near the sea surface: Some issues relevant to remote sensing, *J. Geophys. Res.*, *100*(C7), 13,255–13,266, doi:10.1029/95JC00454.

Dall'Olmo, G., T. K. Westberry, M. J. Behrenfeld, E. Boss, and W. H. Slade (2009), Significant contribution of large particles to optical backscattering in the open ocean, *Biogeosciences*, *6*(6), 947–967.

Dall'Olmo, G., E. Boss, M. J. Behrenfeld, T. K. Westberry, C. Courties, L. Prieur, M. Pujo-Pay, N. Hardman-Mountford, and T. Moutin (2011), Inferring phytoplankton carbon and eco-physiological rates from diel cycles of spectral particulate beam-attenuation coefficient, *Biogeosciences*, *8*(11), 3423–3439, doi:10.5194/bg-8-3423-2011.

Dandonneau, Y., and L. Lemasson (1987), Water-column chlorophyll in an oligotrophic environment: Correction for the sampling depths and variations of the vertical structure of density, and observation of a growth period, *J. Plankton Res.*, *9*(1), 215–234, doi:10.1093/plankt/9.1.215.

D'Asaro, E. A. (2008), Convection and the seeding of the North Atlantic bloom, *J. Mar. Syst.*, *69*(3–4), 233–237, doi:10.1016/j.jmarsys.2005.08.005.

D'Ortenzio, F., and M. R. d' Alcala (2009), On the trophic regimes of the Mediterranean Sea: A satellite analysis, *Biogeosciences*, *6*(2), 139–148.

Dugdale, R. C., and F. P. Wilkerson (1988), Nutrients sources and primary production in the eastern Mediterranean, *Oceanol. Acta*, *9*, 179–184.

Durand, M. D., and R. J. Olson (1996), Contributions of phytoplankton light scattering and cell concentration changes to diel variations in beam attenuation in the equatorial Pacific from flow cytometric measurements of pico-, ultra- and nanoplankton, *Deep-Sea Res. Part II-Top. Stud. Oceanogr.*, *43*(4–6), 891–906, doi:10.1016/0967-0645(96)00020-3.

Estrada, M., C. Marrase, M. Latasa, E. Berdalet, M. Delgado, and T. Riera (1993), Variability of deep chlorophyll maximum characteristics in the Northwestern Mediterranean, *Mar. Ecol. Prog. Ser.*, *92*(3), 289–300, doi:10.3354/meps092289.

Fennel, K., and E. Boss (2003), Subsurface maxima of phytoplankton and chlorophyll: Steady-state solutions from a simple model, *Limnol. Oceanogr.*, *48*(4), 1521–1534.

Gardner, W., I. Walsh, and M. Richardson (1993), Biophysical forcing of particle-production and distribution during a spring bloom in the North-Atlantic, *Deep-Sea Res. Part II-Top. Stud. Oceanogr.*, *40*(1–2), 171–195, doi:10.1016/0967-0645(93)90012-C.

Gardner, W. D., A. V. Mishonov, and M. J. Richardson (2006), Global POC concentrations from in-situ and satellite data, *Deep-Sea Res. Part II-Top. Stud. Oceanogr.*, *53*(5–7), 718–740, doi:10.1016/j.dsr2.2006.01.029.

Gordon, H., and W. McCluney (1975), Estimation of depth of sunlight penetration in sea for remote-sensing, *Appl. Opt.*, *14*(2), 413–416, doi:10.1364/AO.14.000413.

Hense, I., and A. Beckmann (2008), Revisiting subsurface chlorophyll and phytoplankton distributions, *Deep-Sea Res. Part I -Oceanogr. Res. Pap.*, *55*(9), 1193–1199, doi:10.1016/j.dsr.2008.04.009.

IOCCG (2011), *Bio-Optical Sensors on Argo Floats*, edited by Reports of the International Ocean-Colour Coordinating Group, IOCCG, Darmouth, Canada.

Johnson, K. S., S. C. Riser, and D. M. Karl (2010), Nitrate supply from deep to near-surface waters of the North Pacific subtropical gyre, *Nature*, *465*(7301), 1062–1065, doi:10.1038/nature09170.

Karl, D. M. (1999), A sea of change: Biogeochemical variability in the North Pacific Subtropical Gyre, *Ecosystems*, *2*(3), 181–214, doi:10.1007/s100219900068.

Karl, D. M., and R. Lukas (1996), The Hawaii Ocean Time-series (HOT) program: Background, rationale and field implementation, *Deep-Sea Res. Part II-Top. Stud. Oceanogr.*, *43*(2–3), 129–156, doi:10.1016/0967-0645(96)00005-7.

Kitchen, J., and J. Zaneveld (1990), On the noncorrelation of the vertical structure of light-scattering and chlorophyll-a in case-I waters, *J. Geophys. Res.*, *95*(C11), 20,237–20,246, doi:10.1029/JC095iC11p20237.

Letelier, R., R. Bidigare, D. Hebel, M. Ondrusek, C. Winn, and D. Karl (1993), Temporal variability of phytoplankton community structure-based on pigment analysis, *Limnol. Oceanogr.*, *38*(7), 1420–1437.

Letelier, R. M., D. M. Karl, M. R. Abbott, and R. R. Bidigare (2004), Light driven seasonal patterns of chlorophyll and nitrate in the lower euphotic zone of the North Pacific Subtropical Gyre, *Limnol. Oceanogr.*, *49*(2), 508–519.

Lewis, M., W. Harrison, N. Oakey, D. Hebert, and T. Platt (1986), Vertical nitrate fluxes in the oligotrophic ocean, *Science*, *234*(4778), 870–873, doi:10.1126/science.234.4778.870.

Loisel, H., and A. Morel (1998), Light scattering and chlorophyll concentration in case 1 waters: A reexamination, *Limnol. Oceanogr.*, *43*(5), 847–858.

Maranon, E., P. M. Holligan, M. Varela, B. Mourino, and A. J. Bale (2000), Basin-scale variability of phytoplankton biomass, production and growth in the Atlantic Ocean, *Deep-Sea Res. Part I-Oceanogr. Res. Pap.*, *47*(5), 825–857, doi:10.1016/S0967-0637(99)00087-4.

Marty, J. C., J. Chiaverini, M. D. Pizay, and B. Avril (2002), Seasonal and interannual dynamics of nutrients and phytoplankton pigments in the western Mediterranean Sea at the DYFAMED time-series station (1991–1999), *Deep-Sea Res. Part II-Top. Stud. Oceanogr.*, *49*(11), 1965–1985, doi:10.1016/S0967-0645(02)00022-X.

McClain, C. R., S. R. Signorini, and J. R. Christian (2004), Subtropical gyre variability observed by ocean-color satellites, *Deep-Sea Res. Part II-Top. Stud. Oceanogr.*, *51*(1–3), 281–301, doi:10.1016/j.dsr2.2003.08.002.

McGill, D. A. (1969), A budget for dissolved nutrient salts in the Mediterranean Sea, *Cah. Oceanogr.*, *21*, 543–554.

Michaels, A. F., and A. H. Knap (1996), Overview of the U.S. JGOFS Bermuda Atlantic Time-series Study and the Hydrostation S program, *Deep Sea Res. Part II Top. Stud. Oceanogr.*, *43*(2–3), 157–198, doi:10.1016/0967-0645(96)00004-5.

Mignot, A., H. Claustre, F. D'Ortenzio, X. Xing, A. Poteau, and J. Ras (2011), From the shape of the vertical profile of in vivo fluorescence to Chlorophyll-a concentration, *Biogeosciences*, *8*(8), 2391–2406, doi:10.5194/bg-8-2391-2011.

Mitchell, B., and O. Holmhansen (1991), Biooptical properties of Antarctic peninsula waters - differentiation from temperate ocean models, *Deep-Sea Res. Part A -Oceanogr. Res. Pap.*, *38*(8–9), 1009–1028.

Mitchell, B., and D. Kiefer (1988), Variability in pigment specific particulate fluorescence and absorption-spectra in the northeastern pacific-ocean, *Deep-Sea Res. Part A -Oceanogr. Res. Pap.*, *35*(5), 665–689.

Montegut, C. D., G. Madec, A. S. Fischer, A. Lazar, and D. Iudicone (2004), Mixed layer depth over the global ocean: An examination of profile data and a profile-based climatology, *J. Geophys. Res.*, *109*, C12003, doi:10.1029/2004JC002378.

Morel, A. (1973), Diffusion de la lumière par les eaux de mer; résultats expérimentaux et approche théorique, *AGARD Lect. Ser. 61*, pp. 3.1.1–3.1.76.

Morel, A. (1974), Optical properties of pure water and pure sea water, in *Optical Aspects of Oceanography*, pp. 1–24, Academic Press, New York.

Morel, A. (1988), Optical modeling of the upper ocean in relation to its biogenous matter content (case-I waters), *J. Geophys. Res.*, *93*(C9), 10,749–10,768, doi:10.1029/JC093iC09p10749.

Morel, A., and S. Maritorena (2001), Bio-optical properties of oceanic waters: A reappraisal, *J. Geophys. Res.*, *106*(C4), 7163–7180, doi:10.1029/2000JC000319.

Morel, A., L. Lazzara, and J. Gostan (1987), Growth-rate and quantum yield time response for a diatom to changing irradiances (energy and color), *Limnol. Oceanogr.*, *32*(5), 1066–1084.

Morel, A., Y.-H. Ahn, F. Partensky, D. Vaulot, and H. Claustre (1993), Prochlorococcus and Synechococcus: A comparative study of their optical properties in relation to their size and pigmentation, *J. Mar. Res.*, *51*(3), 617–649, doi:10.1357/0022240933223963.

Morel, A., Y. Huot, B. Gentili, P. J. Werdell, S. B. Hooker, and B. A. Franz (2007), Examining the consistency of products derived from various ocean color sensors in open ocean (Case 1) waters in the perspective of a multi-sensor approach, *Remote Sens. Environ.*, *111*(1), 69–88, doi:10.1016/j.rse.2007.03.012.

Morel, A., H. Claustre, and B. Gentili (2010), The most oligotrophic subtropical zones of the global ocean: Similarities and differences in terms of chlorophyll and yellow substance, *Biogeosciences*, *7*(10), 3139–3151, doi:10.5194/bg-7-3139-2010.

Polovina, J. J., E. A. Howell, and M. Abecassis (2008), Ocean's least productive waters are expanding, *Geophys. Res. Lett.*, *35*, L03618, doi:10.1029/2007GL031745.

Ras, J., H. Claustre, and J. Uitz (2008), Spatial variability of phytoplankton pigment distributions in the Subtropical South Pacific Ocean: Comparison between in situ and predicted data, *Biogeosciences*, *5*(2), 353–369.

Roemmich, D., O. Boebel, B. Freeland, B. King, and P.-Y. LeTraon (1999), On the design and Implementation of Argo-An initial plan for a global array of profiling floats.

Sarmiento, J. L., et al. (2004), Response of ocean ecosystems to climate warming, *Global Biogeochem. Cycles*, *18*, GB3003, doi:10.1029/2003GB002134.

Seki, M. P., J. J. Polovina, R. E. Brainard, R. R. Bidigare, C. L. Leonard, and D. G. Foley (2001), Biological enhancement at cyclonic eddies tracked with GOES thermal imagery in Hawaiian waters, *Geophys. Res. Lett.*, *28*(8), 1583–1586, doi:10.1029/2000GL012439.

Siegel, D. A., et al. (2013), Regional to global assessments of phytoplankton dynamics from the SeaWiFS mission, *Remote Sens. Environ.*, *135*, 77–91, doi:10.1016/j.rse.2013.03.025.

Stramski, D., and D. Kiefer (1991), Light-scattering by microorganisms in the open ocean, *Prog. Oceanogr.*, *28*(4), 343–383, doi:10.1016/0079-6611(91)90032-H.

Venrick, E. (1988), The Vertical distributions of chlorophyll and phytoplankton species in the north pacific central environment, *J. Plankton Res.*, *10*(5), 987–998, doi:10.1093/plankt/10.5.987.

Westberry, T. K., G. Dall'Olmo, E. Boss, M. J. Behrenfeld, and T. Moutin (2010), Coherence of particulate beam attenuation and backscattering coefficients in diverse open ocean environments, *Opt. Express*, *18*(15), 15,419–15,425.

Winn, C., L. Campbell, J. Christian, R. Letelier, D. Hebel, J. Dore, L. Fujieki, and D. Karl (1995), Seasonal variability in the phytoplankton community of the north pacific subtropical gyre, *Global Biogeochem. Cycles*, *9*(4), 605–620, doi:10.1029/95GB02149.

Wong, A., R. Keeley, T. Carval, and the Argo Data Management Team (2010), Argo quality control manual, *Tech. Rep.*, Argo Data Management team.

Xing, X., A. Morel, H. Claustre, D. Antoine, F. D'Ortenzio, A. Poteau, and A. Mignot (2011), Combined processing and mutual interpretation of radiometry and fluorimetry from autonomous profiling Bio-Argo floats: Chlorophyll a retrieval, *J. Geophys. Res.*, *116*, C06020, doi:10.1029/2010JC006899.